PHYSICAL REVIEW B **83**, 094112 (2011)

Modeling the iron oxides and oxyhydroxides for the prediction of environmentally sensitive phase transformations

Haibo Guo and Amanda S. Barnard
Virtual Nanoscience Laboratory, Division of Materials Science and Engineering, CSIRO, Australia

(Received 19 October 2010; revised manuscript received 13 January 2011; published 8 March 2011)

Iron oxides and oxyhydroxides are challenging to model computationally as competing phases may differ in formation energies by only several kJ mol^{-1}, they undergo magnetization transitions with temperature, their structures may contain partially occupied sites or long-range ordering of vacancies, and some loose structures require proper description of weak interactions such as hydrogen bonding and dispersive forces. If structures and transformations are to be reliably predicted under different chemical conditions, each of these challenges must be overcome simultaneously while preserving a high level of numerical accuracy and physical sophistication. Here we present comparative studies of structure, magnetization, and elasticity properties of iron oxides and oxyhydroxides using density-functional-theory calculations with plane-wave (PW) and locally-confined-atomic-orbital basis sets, which are implemented in VASP and SIESTA packages, respectively. We have selected hematite (α-Fe$_2$O$_3$), maghemite (γ-Fe$_2$O$_3$), goethite (α-FeOOH), lepidocrocite (γ-FeOOH), and magnetite (Fe$_3$O$_4$) as model systems from a total of 13 known iron oxides and oxyhydroxides, and we used the same convergence criteria and almost equivalent settings to make consistent comparisons. Our results show that both basis sets can reproduce the energetic stability and magnetic ordering, and are in agreement with experimental observations. There are advantages to choosing one basis set over the other, depending on the intended focus. In our case, we find the method using PW basis set the most appropriate, and we combine our results to construct the first phase diagram of iron oxides and oxyhydroxides in the space of competing chemical potentials, generated entirely from first principles.

DOI: 10.1103/PhysRevB.83.094112 PACS number(s): 71.15.Mb, 75.47.Lx, 82.60.−s, 62.20.D−

I. INTRODUCTION

Iron oxides and oxyhydroxides are abundant in nature; they are widespread in soils, waters, and rocks, and are also found in living organisms, air dusts, meteorites, and Martian soils[1] (pp. 1–7). Iron oxides and oxyhydroxides have been the focus of numerous studies in the fields of geology, materials, soil, biology, and environmental sciences, and have broad applications in pigments, magnetic recording devices, medical imaging contrast agents, and heavy metal sequestration absorbents[1] (pp. 2 and 509–523). To date, 13 natural and synthetic iron oxides and oxyhydroxides (in addition to two hydroxides; see Ref. 1, p. 2) have been identified. These polymorphs have complicated structures (poor crystallization, ordering of vacancies, partial site occupancy), undergo a range of phase transformations, have characteristic magnetization states, and participate in a number of different types of interactions with contaminants and adsorbates. Given their ubiquity, it is surprising to find that the structures of some iron oxides and oxyhydroxides remain poorly understood, even after years of studies and numerous debates. In addition, size effects introduce a further complication, especially when we approach nanometer regimes, as shown in a recent review of the structure complexity,[2] in which the authors showed that particle size, hydrous and hydrated environments, and synthesis processes all affect the observed structure. Collectively, these complicated issues have fueled constant interest in iron oxides and oxyhydroxides over the past decades.

Like many materials, the development of characterization technologies and new samples often sparked renewed debates and led to new questions. One example is the debate on the origins of magnetite found in meteorites and magnetotactic bacteria. The magnetite nanocrystals from the Martian meteorite ALH84001 share many features with that from magnetosomes in terrestrial magnetotactic bacteria.[3] The similarities include unusual morphology, chemical purity, and crystallographic perfection. The similarities led to the proposal that the magnetite nanocrystals from the Martian meteorite were produced by biogenic processes, therefore they provided strong evidence of life on early Mars.[4,5] This proposal was later questioned[6,7] and even dismissed[8] because inorganic processes can also produce similar morphologies. However, the debate triggered new studies seeking reliable methods to identify origins of magnetite nanocrystals, and crystal size distributions[9] and oxygen isotope fractionation[10] have now been proposed to discriminate inorganic from organic origins.

In recent years, computational modeling has opened up another potential way to solve the pending questions about iron oxides and oxyhydroxides. It generally requires electronic-level modeling methods to capture the magnetization states of iron oxides and oxyhydroxides. And in this respect, density-functional theory (DFT)[11] is able to solve electronic structures with desired accuracy at affordable computational cost. While DFT implementations have been routinely used to solve a wide range of problems in materials science, iron oxides and oxyhydroxides are particularly challenging for a number of reasons. First, the energy differences between different solid phases or magnetization states may be as low as several kJ mol^{-1}, which is close to the resolutions of most DFT calculations, and necessitates energetic convergence criteria on the order of a few meV. Secondly, the underestimation of band gaps by DFT makes it difficult to depict the correct electronic structures of iron oxides and oxyhydroxides, most of which are semiconductors. A remedy to this problem is to include on-site Coulomb interaction to describe the strongly correlated 3*d* electrons.[12] Thirdly, the structures of iron oxides and oxyhydroxides may have partially occupied sites, or long-range ordering of vacancies (as in maghemite), which need large super cells and, accordingly, heavy computation loads. Fourthly, the charge ordering and associated symmetry change in magnetite below the Verwey transition temperature[13–19] are computationally intractable. Working models proposed for charge ordering generally go beyond most DFT implementations. Fifthly, some iron oxyhydroxides have loose structure, for example, lepidocrocite (γ-FeOOH), where the binding between layers relies on week hydrogen bonds and dispersive forces, which, however, are poorly described in DFT. And finally, various magnetization states in iron oxides and oxyhydroxides usually lead to slow convergence in calculations.

The challenges of iron oxides and oxyhydroxides make computational modeling and simulation nontrivial tasks, and work in this area tends to be sparse and sporadic. Despite the difficulties, DFT calculations have been applied to some iron oxides and oxyhydroxides in the past.[17,18,20–31] These calculations incorporated different approximations, basis sets, and computational settings. It is therefore difficult to compare their accuracy and assess the methodology and algorithms, even though such a comparison is highly desirable for selecting computation tools in studying this difficult system. It also means that a systematic comparison between studies is not necessarily reliable, and cross-comparisons of different materials (such as those provided in phase diagrams) is not possible. However, when we seek to overcome this problem, we are confronted with the question of which is the most appropriate technique to employ.

In this study, we will present a comparative study between two implementations of DFT in calculating thermodynamic, magnetic, and elastic properties of iron oxides, and assess the efficiency, accuracy, and convergence, based on five iron oxides and oxyhydroxides, including hematite (α-Fe_2O_3), maghemite (γ-Fe_2O_3), goethite (α-FeOOH), lepidocrocite (γ-FeOOH), and magnetite (Fe_3O_4). Based on this large and consistent set of results, we are in a position to present the first environmentally sensitive phase diagram of iron oxides and oxyhydroxides, generated entirely from first principles, for predicting the thermodynamically stable structure as a function of the supersaturation of oxygen and/or hydrogen.

II. COMPUTATIONAL METHODS

A major difference among implementations of DFT is the choice of basis sets to expand the state space. Electronic wave functions can be constructed by linear combination of delocalized plane waves (PW's), or locally confined atomic orbitals (LCAO's). The two basis sets have their advantages and disadvantages.[32,33] PW's have definite mathematical forms, are easy to implement, and have systematic convergence over cutoff energies, but their delocalized nature prevents linear scaling with the system size. LCAO's are flexible in terms of shape, size, and range, require much fewer orbitals compared to PW's, and they are localized and thus suitable for spatial partition and linear scaling algorithms, but they lack a systematic convergence and require extra effort to tune the LCAO parameters. We choose the DFT implementations in VASP (Vienna Ab initio Simulation Package)[34,35] for the PW basis set, and SIESTA (Spanish Initiative for Electronic Simulations with Thousands of Atoms)[36,37] for the LCAO basis set.

It is a known failure of the local-density approximation (LDA) or the local-spin-density approximation (LSDA) to accurately predict the ground state of bulk iron, while the generalized gradient approximation (GGA) can reproduce the ferromagnetic body-centered cubic (bcc) ground state. [38] Therefore, in our study, we choose GGA (in the form of Perdew, Burke, and Ernzerhof[39]) to describe electron-electron interactions. For consistency, we use the same exchange-correlation functionals for both PW- and LCAO-based implementations, thereby enabling a complementary and detailed comparison between the two basis sets to assist others in this field.

A. Pseudopotentials

In this study, we use pseudopotentials to describe core electrons and nuclei. For the PW basis set, we use the projector augmented wave (PAW) potentials from the pseudopotential libraries shipped with VASP. The reference states of valence electrons for generating the pseudopotentials of Fe is $3d^7 4s^1$. The core radii are 2.30, 1.1, and 1.52 Bohr for Fe, H, and O, respectively. Nonlinear core corrections are included for Fe with radius of 2.0 Bohr.

For Fe, the 3*d* electron orbital overlaps with 3*s* and 3*p* core orbitals in real space, and has a small core radius of approximately 0.7 Bohr. The 4*s* and 4*p* orbitals extrude further away from the nucleus, with radii of approximately 2 Bohr. These different core radii make it difficult to assign a common cutoff to all the orbitals, due to the short core radius of the 3*d* orbital ($\sim$0.7 Bohr), which requires a very large cutoff of PW's (about 11000 eV) to converge the energy in 3 meV/at.[40] One practice to eliminate the difference in core radii is to include 3*s* and 3*p* as semicore states in place of the 4*s* and 4*p* states, respectively. In this way, the reference state is not neutral (one 4*s* electron or two 4*s* electrons are excluded, assuming the ground state is $3d^7 4s^1$ or $3d^6 4s^2$), which is acceptable under the pseudopotential scheme. It is therefore possible to generate high-quality pseudopotentials with small core radii of around 0.6–0.9 Bohr. The hard pseudopotentials can accurately reproduce all-electron calculations to excited states, but are computationally demanding. However, it has been previously shown that the gain in quality of the calculation is not apparent when semicores are included in Ti and Cu.[41] To reduce the computation cost, settings of $\sim$2 Bohr radii have been found to be a good compromise between efficiency and cost. The soft pseudopotentials often produce acceptable results in calculating lattice parameters, magnetization, and electronic structures.

For the LCAO basis set, we generate norm-conserving pseudopotentials according to the revised scheme of Troullier and Martins.[42] A potential generated with the reference valence state of $3d^6 4s^2$, core radii of 2.0 Bohr, and partial core radius of 0.7 Bohr was used in previous studies.[43,44]

Since we wish to compare with our PW calculations, we have chosen the same reference states for Fe ($3d^7 4s^1$). According to our convergence tests, the core radii are 2.0 Bohr for Fe, 1.1 Bohr for O, and 0.8 Bohr for H, smaller than those core radii of the PAW potentials for the PW basis set. Nonlinear core corrections are included for both Fe and O. We found that the nonlinear core radius of 0.7 Bohr provides the best match between pseudocore electron density and all-electron core-electron density. The pseudopotential of Fe generated with the same configurations has been used in studies of the structure and magnetic properties of iron.[44,45] The nonlinear core radius of O is 0.7 Bohr, which is the same as that in Ref. 46. We test the transferability of the pseudopotentials by comparing atomic energies of excited states from pseudopotentials and from all-electron calculations.

It is important to point out that a different nonlinear core radius is used for Fe, and nonlinear core correction is excluded for O in PAW potentials. These differences reflect the degree of compromise between efficiency and transferability. Fortunately, the provision of a standard pseudopotential database (by VASP) allows for considerable testing in a large variety of situations, and the norm-conserving pseudopotentials for LCAO have been tested in the above-mentioned references. Therefore, we are confident that both sets of pseudopotentials should represent core electrons of Fe, H, and O, and are adequate for this comparative study.

B. Basis sets

PW's have a definite mathematical formula with no adjustable parameters. LCAO-based basis sets use the so-called pseudoatomic orbitals (PAO's) whose shape, size, and range are configurable. The PAO's are mathematical functions with adjustable parameters, which must be optimized for specific systems, and the quality of the PAO's is critical to the simulation results of LCAO basis sets. In the present study, we have optimized our PAO's by comparing simulated and known properties of simple structures, specifically the lattice parameter of bulk bcc Fe, and the bond lengths of H_2 and O_2 molecules.

The PAO's in the present study (for all three elements) are of double-ζ plus polarization (DZP). The dimensionless parameter split-norm, which determines the splitting of different ζ functions, was set to 0.28 for Fe, 0.24 for O, and 0.65 for H. The large split-norm of H is in accordance with the large variation in the effective spatial extent of hydrogen in charged states. A similar value of 0.5 was employed during a study of the pressure effects on hydrogen bonds, as reported in Ref. 47. Soft confinement has been applied according to the scheme proposed in Ref. 48 to avoid discontinuity of the functions at the cutoff distance. The parameters for generating the PAO's are summarized in Table I. In the DZP scheme, the numbers of PAO's per atom are 17 for Fe, 13 for O, and 3 for H. The results of bulk Fe and the gas molecules (H_2, O_2, and H_2O) used to construct our basis sets are provided in Sec. III.

C. GGA + U parameter

The strong correlation effects of iron $3d$ electrons lead to splitting of d bands. Depending on the relative positions of oxygen $2p$ and iron $3d$ orbitals in valence bands, iron oxides and oxyhydroxides may be semiconducting or metallic[1], (pp. 115–117). Both GGA and LDA tend to overdelocalize electrons and underestimate correlation effects and band gaps. Model Hamiltonian approaches are often used in such strongly correlated systems.[49] In these models, electrons hopping between atoms experience the effective Coulomb interaction U, which is defined as the energy cost for moving an electron between two atoms that both initially had the same number of electrons, or $U = E_{n+1} + E_{n-1} - 2E_n$, where E_n is the energy of an atom with n $3d$ (for transition metals) or $4f$ (for rare-earth elements) electrons.[49] These energy fluctuations result in the formation of band gaps. As implementation of the model Hamiltonian approaches in DFT, the LDA + U (or GGA + U) method[12,50] includes on-site Coulomb interactions among strongly correlated electrons.

TABLE I. PAO parameters of Fe, O, and H. The r_{c1} and r_{c2} are radii of double-ζ and polarization orbitals, V is a soft-confinement potential, and r_i is the inner radius of the soft confinement. "polar." represents polarization orbitals.

	r_{c1} (Bohr)	r_{c2} (Bohr)	V (Ry)	r_i (Bohr)
Fe $3d$	4.229	2.292	50	3.81
Fe $4s$	6.800	5.363	150	6.12
Fe polar.	6.800		150	6.12
O $2s$	5.000	2.580	0	
O $2p$	6.500	2.497	0	
O polar.	3.923		104.3	0.00
H $1s$	4.971	1.771	2.07	0.00
H polar.	4.988		0.89	0.00

We point out that there exist alternative approaches to solve or alleviate the band-gap problem of DFT, including hybrid HF-DFT (Hartree-Fock-DFT) functionals[51,52] and self-interaction correction.[53,54] These approaches (including the aforementioned DFT + U) are being extensively tested in a large variety of chemical environments and becoming widely implemented. Particularly for strongly correlated systems, hybrid functionals have been shown to properly describe the magnetic coupling in and band gaps of NiO,[55] UO_2,[56] CeO_2 and Ce_2O_3,[57] plutonium oxides,[58] and several strongly correlated solids.[59] Various hybrid functionals have been developed and actively tested with other hybrid functionals and pure functionals.[60,61] Among the recent developments of hybrid functionals, the range-separated hybrids[59,62–64] and Heyd-Scuseria-Ernzerhof hybrid functional[65–68] are very promising in tackling the correlation effects in solids. Hybrid functionals often give acceptable thermochemical results owing partly to their semiempirical nature and the fitting procedure (such that the amount of exact exchange can be tuned to fit known physical and chemical properties). With the increasingly available options, it is, however, desirable to select those density-functional approximations of nonempirical constraint satisfactory with least-fitting parameters.[69] Choices of the approaches may depend on the availability of implementations or computational cost. In this study, we have chosen DFT + U to account for the band-gap problems of DFT because it is implemented in both computation packages (VASP and SIESTA) that are used herein. There are, of course, many other computation packages that use PW and LCAO basis sets with a different compromise between accuracy and computation cost. Both packages that we use for this study have users of broad interest, ranging from physics, chemistry, materials science, and biology. They thus should serve as robust computational tools for our study.

For the strongly correlated systems, the improvements to band-structure calculations provided by DFT + U are substantial.[50] To demonstrate this, we test the GGA + U methods in the calculations of bulk Fe, iron oxides, and oxyhydroxides in both PW and LCAO methods. Both packages have implemented the GGA + U method based on a simplified rotationally invariant formulation by Dudarev *et al.*[50] In this implementation, only the effective Coulomb repulsion $U_{\mathrm{eff}} = U - J$ is significant. In our study, the on-site Coulomb interactions are included only for strongly correlated Fe $3d$ electrons, but not for the electrons of O or H, or other types of electrons of Fe.

The DFT + U method has previously been employed to study magnetite,[17,18] hematite,[20,22,70] goethite,[29] and maghemite,[31] for which the parameter U varies between 2 and 5 eV. Cococcioni and Gironcoli suggested U_{eff} of bulk iron to be ~2.2 eV using a linear-response approach;[71] Anisimov and Gunarsson gave rather large U_{eff} of about 6 eV.[49] Rollmann *et al.* recommended U_{eff} of 3.0 eV through their study of the electronic structure of hematite.[22] Punkkinen *et al.* suggested a much smaller value (~1.0 eV) for hematite, designed to reproduce experimentally observed features of the electronic structure, such as the crystal-field-induced band splitting.[20] Grau-Crespo *et al.* used $U_{\mathrm{eff}} = 4.0$ eV in the study of vacancy ordering of maghemite.[31] The difference may originate from implementations of the DFT + U method, pseudocore configurations, and even basis sets. In the present study, the parameter of U_{eff} is chosen so that the calculated band gaps and lattice parameters both match the experimental values. We found that $U_{\mathrm{eff}} = 4.5$ eV provides the best match the experimental band gaps of hematite (see Sec. III C) and goethite (not shown), and acceptable lattice parameters of all the iron oxides. The same U_{eff} was used for all the iron oxides for consistency.

It is worth noting that standard DFT (LDA or GGA) reproduces thermodynamic properties very well, sometimes exceeding the predictions of the DFT + U method in comparison to experiments. However, DFT + U methods provide much more accurate predictions of electronic structures. Ideally, first-principles methods should accurately predict both thermodynamic and electronic properties, but this remains a goal of those involved in the development of new density functionals. In our calculations, we compare the results of GGA + U with GGA to assist others in selecting the most appropriate approach for their work.

D. Computational settings

To facilitate a cross-comparison, we have used consistent settings for all the iron oxides in both basis sets. The k points for sampling over the Brillouin zone were generated using the Monkhorst-Pack scheme.[72] For a primitive cell of bcc Fe, a k-mesh grid of $23 \times 23 \times 23$, which corresponds to 364 irreducible k points in the first Brillouin zone, can achieve convergence of total energy in 2 meV/at when using the PW basis set. For the LCAO basis set, a k grid of $17 \times 17 \times 17$ can reach the same convergence of energy, and the number of k points is 2457. One immediately notices the large difference in the numbers of k points in the PW and LCAO basis sets. This is due to the different symmetrization treatments in the two programs. The VASP code utilizes crystal symmetries to calculate the charge density, forces, and stresses. The symmetry elements of the crystal structure greatly reduce the number of necessary k points for adequate sampling. The SIESTA code is designed for large systems, as its name indicates, and symmetry constraints are usually excluded. SIESTA only trims a small amount of redundant k points from the constructed grid. Alternatively, SIESTA uses molecular-dynamics (MD) algorithms for geometry optimization over an auxiliary supercell. This difference in symmetrization leads to a very different number of k points used in sampling the band energies, however the convergence criteria of k-mesh density with respect to total energies are set to 1–2 meV/at in both basis sets. The sizes of k mesh and numbers of k points used in the calculations are shown in Table II.

In the PW basis set, we find that a PW cutoff of 800 eV can achieve convergence in the total energies to below 1.0 meV/at for all five iron oxides and oxyhydroxides considered in our study. For bulk Fe, a smaller cutoff (600 eV) is able to achieve the same convergence. In the calculations of isolated O_2, H_2, and H_2O molecules, the PW cutoffs are 850, 600, and 850 eV, respectively. With these cutoffs, the difference in total energies can be reduced to less than 1 meV/at, which is the limiting resolution of the DFT implementation. SIESTA uses a finite real-space grid over which integrations are performed to calculate energies, forces, stresses, and dipoles. The fineness of this finite grid is determined by a cutoff value, which is equivalent to the PW cutoff in the PW basis set. There are subtle differences between these equivalent settings across the two basis sets. In the LCAO basis set, wave functions are constructed using atomic orbitals, and the cutoff should only affect the accuracy of integration; in the PW basis sets, the plane waves are also used to construct the valence wave functions, so the cutoff has a larger impact on the quality of calculations. After the convergence tests, we chose cutoffs of 5130 eV for bulk Fe, 4080 eV for O_2, 2040 eV for H_2, and 6800 eV for all five iron oxides and oxyhydroxides, so that the total energies converge below 2 meV/at.

Gaussian (in the PW basis set) or Fermi-Dirac (in the LCAO basis set) distribution functions are used for electronic

TABLE II. Sizes of k meshes and numbers of k points in the calculations using the PW and LCAO basis sets. The numbers in the PW column are the numbers of irreducible k points in the first Brillouin zone, and the numbers in the LCAO column are the numbers of trimmed k points.

	k grid	PW	LCAO
magnetite	4 × 4 × 4	10	44
hematite	4 × 4 × 4	13	64
maghemite	2 × 2 × 2	1	8
goethite	4 × 6 × 4	24	60
lepidocrocite	8 × 4 × 8	32	150

occupations for the molecules (H_2, O_2, and H_2O), iron oxides, and oxyhydroxides; Methfessel-Paxton functions of order 1 are used for bulk iron. The smearing width or electronic temperature has been set to 0.03 eV for all the iron oxides and oxyhydroxides, and 0.05 eV for bulk Fe, in both basis sets; a relatively small value (0.15 eV) is used for the isolated O_2 molecule, and large values (0.4 or 0.5 eV) are used for the isolated H_2 and H_2O molecules (in both basis sets). These values are chosen so that the energies diverge by less than 2 meV/at compared with smaller smearing widths.

Energy minimizations to all the structures are conducted using conjugate gradient (CG) algorithms with the force convergence of 0.005 eV/Å. For the iron oxides and oxyhydroxides, geometry optimizations of unit cells are done with a convergence criterion of 0.005 GPa for the stress tensor components. For the isolated molecules (O_2, H_2 and H_2O), a large supercell of $10 \times 10 \times 10$ Å^3 is used (in both basis sets).

E. Magnetization states

Iron oxides and oxyhydroxides undergo magnetic phase transitions at different temperatures. Most of them are antiferromagnetic or ferrimagnetic at temperatures below their Néel or Curie temperatures. Magnetite and maghemite are ferrimagnetic; hematite, goethite, and lepidocrocite are antiferromagnetic[1] (p. 123). In this study, we consider alternative magnetization states in addition to those observed experimentally. By comparing the energetic stability of different magnetization states, we are able to test the validity of our calculations. In general, a non-spin-polarized state, a ferromagnetic state, and several other initial spin-polarization states are included. However, we only consider collinear magnetization states, which are most commonly observed in iron oxides and oxyhydroxides at low temperatures.

For consistency, we have also included spin polarizations when calculating the properties of the isolated molecules, even though H_2 and H_2O are nonmagnetic (or diamagnetic). In both PW and LCAO calculations, the net spin moments of H_2 and H_2O are zero, in agreement with experimental observations. The spin moment of O_2 is $2.0\mu_B$ using both PW and LCAO basis sets.

F. Elastic properties

In this study, we calculated bulk moduli of each solid material by fitting to Birch-Murnagham equation of state.[73] In addition, we calculate the elasticity tensors of bulk Fe, iron oxides, and oxyhydroxides using a finite-difference method. In this method, a series of strains are applied to the equilibrium unit cell, the total energies of the strained structures are calculated, and the elasticity tensor components c_{ij} are calculated through

$$E = E_0 + \frac{1}{2}\sum c_{ij}\epsilon_i\epsilon_j, \tag{1}$$

where E is the total energies of strained structures, E_0 is the total energy of equilibrium structure with zero stresses, and ϵ is the applied strain. The subscripts i and j are of matrix notations[74] (p. 134). The strains are grouped into a number of transformations, which are chosen in accordance with the crystal symmetry of the structures. For each transformation, six strains of ±0.015, ±0.010, and ±0.005, in addition to the equilibrium structure, are used for linear least-squares fitting to calculate the c_{ij} tensor components.

We developed a computer program to calculate elastic constants of crystals by using *ab initio* packages as back ends. Since this method only requires total energies, which can be calculated using many computation packages, we can make consistent comparisons by using the same strains. This method and program have been previously tested in calculating elastic constants of Co[75] and Ni-B alloys.[76]

III. RESULTS AND DISCUSSIONS

In the following sections, we will focus on presenting results of our detailed comparisons between the PW and LCAO basis sets, as well as the physical comparisons being made in energetic stability, lattice parameters, elastic properties, and magnetization states of our collection of iron oxides and oxyhydroxides.

A. Bulk Fe

The ground state of bulk iron is of bcc structure (space group $Im\bar{3}m$, No. 229) and ferromagnetic. Fe is a well-behaved system within the framework of standard DFT-GGA, which predicts correctly thermodynamic properties such as energetic stability and lattice parameters. With on-site Coulomb interactions, first-principles calculations can improve the predictions to electronic band structures. As mentioned above, the parameter U_{eff} may vary from below 1 eV to about 6 eV, depending on the methods and interpretations.[45,49,71,77,78] As our focus is on thermodynamic properties, we apply mild on-site Coulomb interactions with $U_{\mathrm{eff}} = 1.0$ eV when calculating the properties of bulk iron. We choose this value of U_{eff} because it improves the predictions of the lattice constant and cohesive energy in PW basis set (see Fig. 1 and Table III). In general, we find that the lattice constant of Fe increases almost linearly with U_{eff}. This is because on-site interactions alter charge density around Fe atoms, weakening the metallic bonding strength, similar to that observed in NiO.[50] The spin moment, which is sensitive to changes of atomic volume, also increases with U_{eff}.

The calculation results are summarized in Table III. Both calculations using PW and LCAO basis sets reproduce experimental lattice constants within 1.5%. All the calculations overestimate cohesive energy with respect to experimental measurement. LCAO overestimates by about 1.5 eV. The difference between calculation and experiment is much smaller in PW basis set. GGA using PW overestimates by about 0.5 eV, while GGA + U reduces the overestimation to about 0.1 eV. The calculations of the spin polarization moments (not including orbital moments) compare favorably with experiments, at around $2.5\mu_B$.

For the calculations of the bulk moduli, GGA + U using PW best matches the results from experiments, while we find that other methods overestimate the values by between 8% (GGA with LCAO) and 18% (GGA with PW). Both fitting errors and temperature effect may contribute to the difference between calculations and experiments, because bulk moduli are calculated at ground state from Birch-Murnagham equation

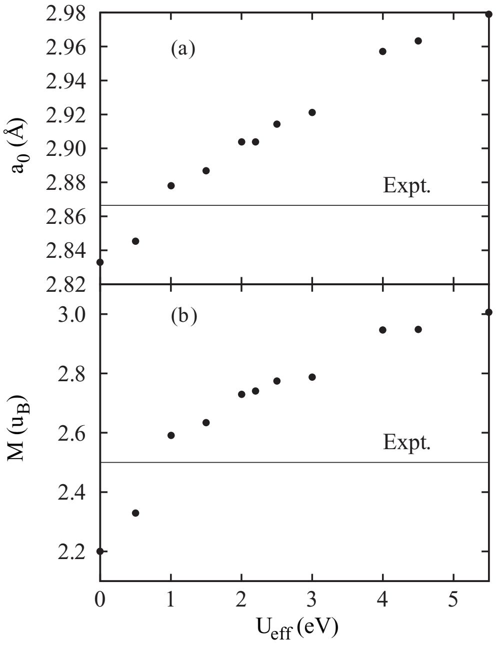

FIG. 1. Dependence of (a) lattice parameter and (b) spin moment on U_{eff} in PW-based calculations. Experimental values are marked with horizontal lines.

TABLE IV. Calculated properties of gas molecules. L stands for bond length, E for binding energy, E_f for formation enthalpy, and α for bond angle of H-O-H in H_2O.

	PW	LCAO	Expt.[a]
$L_{\text{H-H}}$ (Å)	0.7500	0.7465	0.7414
$E_{\text{H-H}}$ (eV/bond)	4.538	4.749	4.521
$L_{\text{O-O}}$ (Å)	1.2323	1.2422	1.2074
$E_{\text{O-O}}$ (eV/bond)	6.8074	6.2181	5.1697
$L_{\text{O-H}}$ (Å)	0.9575	0.9754	0.9575
$\alpha_{\text{H-O-H}}$ (°)	104.46	104.93	104.51
$E_f(H_2O)$ (kJ mol^{-1})	−243.8	−234.3	−241.8

[a] Ref. 86, pp. 9–22, 9–24, 9–57, and 9–58.

of state, and experiments are conducted at the thermodynamic standard state. For the calculations of the elasticity tensors, we find that GGA using LCAO provides the best overall results, and other methods either underestimate c_{44} or overestimate c_{11} and c_{12} significantly. In particular, the components of the elasticity tensor calculated using GGA and the PW basis set can be considerably different from the experimental values, especially in the case of c_{11}, but they are very close to those in recent calculations using exact muffin-tin orbitals and Perdew-Burke-Ernzerhof (PBE) functionals.[79] However, GGA + U tends to underestimate c_{44} considerably using both PW and LCAO. The differences between calculations and experiments may include defects in single-crystal Fe being measured, extrapolation to ground state, anharmonic effects, and numerical error in the calculations.

As shown in Table III, GGA + U generally offers a small improvement over GGA in calculating the lattice constant and cohesive energy of bulk iron, at the expense of the apparent underestimation of c_{44}.

B. Gas molecules

As stated above, we have calculated the binding energies and bond lengths of H_2 and O_2 and the bond angles of H_2O (see Table IV). Except for the binding energy of O_2, the calculation results match experimental values within 2.5%. The significant overestimation of binding energy of an oxygen dimer (and all other first-row elements with more-than-half-filled p orbitals) by DFT is due to the insufficient description of exchange energy and the lack of error canceling because of different electron shapes of O and O_2.[84,85] Since the energy of an oxygen dimer tends to be canceled out when calculating the energy differences between different phases, this overestimation is unproblematic in calculations of compounds, bulk iron oxides, and oxyhydroxides.

TABLE III. Calculation results of ferromagnetic Fe in bcc structure. a_0: equilibrium lattice constant; E_c: cohesive energy; B_0: bulk modulus; M: spin polarization moment per Fe atom; c_{ij}: elasticity tensor components. Statistic errors of linear least-square fitting are included for c_{ij}.

	PW		LCAO		
	GGA	GGA + U	GGA	GGA + U	Expt.
a_0 (Å)	2.833	2.878	2.868	2.909	2.87[a]
E_c (eV)	4.94	4.36	5.97	5.64	4.28[b]
M (μ_B)	2.20	2.79	2.31	2.67	(about 2.5)
B_0 (GPa)	198.4	164.6	182.1	188.0	168.3[c]
c_{11} (GPa)	302.9 ± 1.4	207.4 ± 0.1	262.3 ± 8.1	230.6 ± 1.5	243.1,[d] 239.3,[e] 297.8[f]
c_{12} (GPa)	151.6 ± 1.5	151.0 ± 0.2	126.8 ± 14.7	165.0 ± 1.8	138.1,[d] 135.8,[e] 141.9[f]
c_{44} (GPa)	97.8 ± 1.4	58.9 ± 0.2	97.0 ± 1.8	73.1 ± 1.4	121.9,[d]120.7,[e] 106.7[f]

[a] Ref. 80, p. 23.
[b] Ref. 81.
[c] Ref. 80, p. 59.
[d] Ref. 82.
[e] Ref. 83.
[f] Ref. 79.

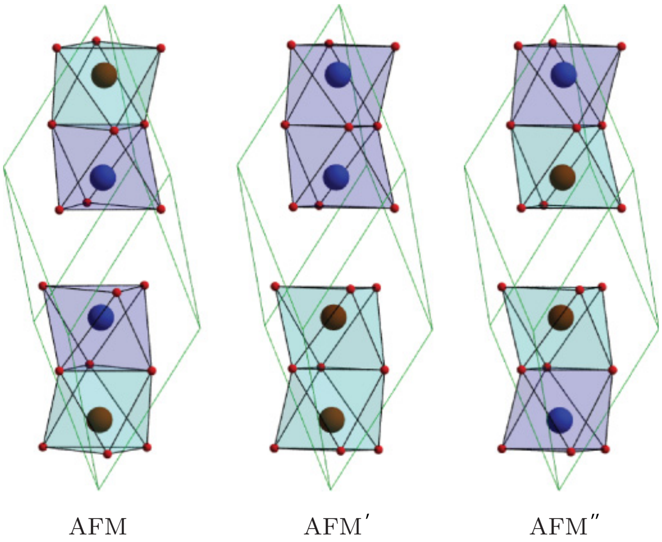

FIG. 2. (Color online) Antiferromagnetic configurations of hematite. Antiparallel spin moments are in blue and cyan. The rhombohedral unit cell is marked by green lines.

C. Hematite (α-Fe_2O_3)

Hematite belongs to the trigonal space group of $R\bar{3}c$ (No. 167), and is isostructural with corundum Al_2O_3 or ilmenite ($FeTiO_3$). It is one of the most thermodynamically stable and abundant phases among all of the iron oxides and oxyhydroxides[1] (p. 6). Each rhombohedral unit cell contains four Fe atoms, distributed over two interlayer spaces of cation layers. Hematite is antiferromagnetic (AFM) with all Fe ions in the same close-packing layer (perpendicular to the trigonal axis [0001]) having parallel spin moments, and different layers having antiparallel spin moments, denoted as AFM (see Fig. 2). At low temperatures below about 250 K, the spin moments change direction from perpendicular to parallel to the trigonal axis, keeping the antiferromagnetic configuration,[87] and no reports have found that the crystal structure changes at this magnetic transition. To validate our calculation results on hematite, we have included another two types of antiferromagnetic configurations in which Fe ions in the same layer have antiparallel spin (denoted as AFM′ and AFM″; see Fig. 2), a ferrimagnetic (FiM), a ferromagnetic (FoM), and a nonmagnetic (NM) configurations.

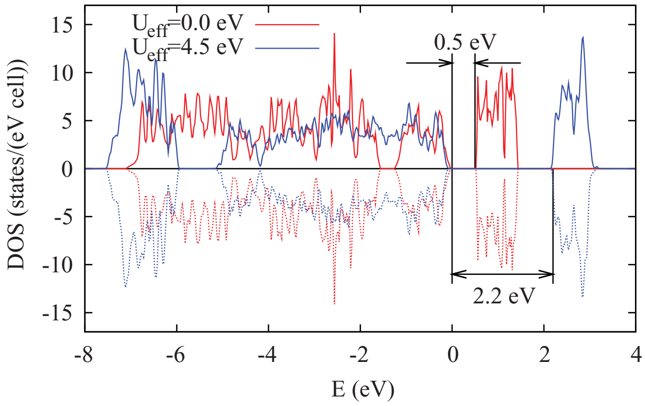

FIG. 3. (Color online) Density of states of antiferromagnetic (AFM) hematite. Up- and down-spin states are in solid and dashed lines, respectively. The numbers are band gaps for $U_{\mathrm{eff}} = 0$ eV (no correction of on-site interaction) and $U_{\mathrm{eff}} = 4.5$ eV. The Fermi energy is shifted to 0 eV. The density of states is calculated with fully relaxed structures.

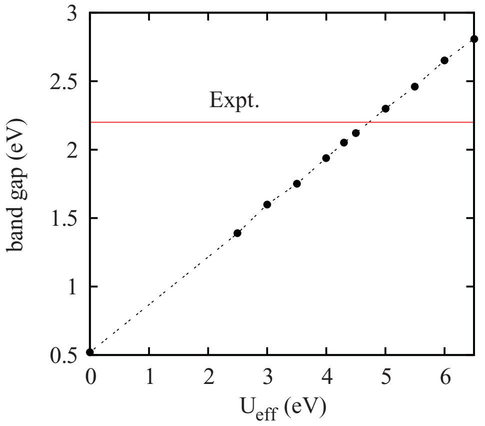

FIG. 4. (Color online) Dependence of band gap of hematite on U_{eff} in GGA + U calculations.

Ignoring on-site interactions leads to significant underestimation to the band gap (0.5 eV in calculation compared with 2.2 eV from experiment; see Fig. 3). We find that the calculated band gap increases linearly with U_{eff}, as shown in Fig. 4. In choosing the parameter U_{eff} in GGA + U calculations, we fit the band gap to experimental value [about 2.2 eV (Ref. 1)]. To reproduce the experimental value of 2.2 eV, U_{eff} should be 4 ∼ 5 eV. We have therefore adopted $U_{\mathrm{eff}} =$ 4.5 eV, and used this value consistently in our calculations to all the iron oxides and oxyhydroxides (in addition to hematite) using both PW and LCAO basis sets.

The calculated thermodynamic and elastic properties for hematite are listed in Tables V and VI. We see that both PW and LCAO correctly predict the lowest-energy state of the AFM configuration, in agreement with experimental observations. The calculated lattice parameters match experimental values within 3% for this stable configuration. In this case, we find that PW does a better job of reproducing the lattice parameters than LCAO. In both basis sets, the lattice parameters from GGA + U are slightly larger than those from GGA. The largest difference between the two basis sets is the spin polarization moment of the metastable ferromagnetic state (FoM). In PW, the average spin moment is low (1.00μ_B), in contrast with that in LCAO, where the average spin moment is high (3.42μ_B). Both basis sets agree on the energetic order of the magnetization states, predicting that AFM < FiM < FoM < NM (formation energy increasing), but differ about the two antiferromagnetic states (AFM′ and AFM″).

In the case of hematite, the calculated elastic constants using PW compare favorably with those determined using LCAO. Both basis sets give almost zero c_{14} (within numerical errors), while the calculation results of c_{44} differ by ∼30 GPa between PW and LCAO. We notice that GGA + U produces larger values of c_{33} than GGA using both PW and LCAO basis sets, indicating that on-site interactions strengthen bonding along the trigonal axis. All the elasticity tensors satisfy the elastic stability condition, which means hematite is elastically stable in all four calculations.

TABLE V. Calculated thermodynamic properties of hematite. The numbers in parentheses are the errors in percent compared with experimental values. The spin polarization is total spin moment of a unit cell (so that antiferromagnetization has exactly zero spin moment) divided by the number of Fe atoms. The energetically most stable magnetic states are in the first row of each basis set (PW or LCAO), GGA+U calculations start from the energetically most stable magnetic states. FoM stands for ferromagnetic, FiM for ferrimagnetic, AFM for antiferromagnetic, and NM for nonmagnetic. GGA + U corresponds to the magnetization state of the lowest energy in GGA calculations.

		a (Å)	c (Å)	M (μ_B)	E_f (kJ mol^{-1})
PW	AFM	5.005 (−0.6)	13.884 (+1.0)	0.00	−628.0
	AFM′	4.841 (−3.8)	13.183 (−4.1)	0.00	−561.2
	AFM″	5.044 (+0.2)	13.850 (+0.7)	0.00	−588.1
	FiM	4.977 (−1.1)	13.707 (−0.3)	1.50	−592.3
	FoM	4.783 (−5.0)	13.333 (−3.0)	1.00	−569.3
	NM	4.733 (−6.0)	13.511 (−1.8)		−543.0
	GGA + U	5.074 (+0.8)	13.874 (+0.9)	0.00	
LCAO	AFM	5.091 (+1.1)	13.995 (+1.8)	0.00	−676.8
	AFM′	5.167 (+2.6)	13.781 (+0.2)	0.00	−640.1
	AFM″	5.137 (+2.0)	13.955 (+1.4)	0.00	−638.5
	FiM	5.056 (+0.4)	13.809 (+0.4)	1.50	−629.6
	FoM	5.026 (−0.2)	13.955 (+1.5)	3.42	−585.6
	NM	4.751 (−5.6)	13.755 (−0.0)		−536.7
	GGA + U	5.183 (+3.0)	14.072 (+2.3)	0.00	
Expt.[a]		5.034	13.752	0.00	−823 ∼ −828

[a] Measured at room temperature and 0.1 MPa. Ref. 1, pp. 11 and 187.

D. Maghemite (γ-Fe$_2$O$_3$)

Maghemite occurs as a weathering product of magnetite, and resembles magnetite in structure and magnetic properties. The Fe ions are all in the trivalent state, with balancing vacancies to maintain charge neutrality. The crystal structure of maghemite has been characterized to be cubic, the same as magnetite, with partially occupied vacancies at octahedral sites.[88,89] Depending on the ordering of cation vacancies, maghemite may be classified in either cubic ($Fd\bar{3}m$ or $P4_332$) or tetragonal ($P4_12_12$) space groups. Somogyvri *et al.* reported long-range ordering of vacancies in powder neutron and x-ray diffraction (XRD) of nanocrystalline needle-shaped maghemite, and classified maghemite to be in the $P4_12_12$ space group.[89] Using powder neutron diffraction, Greaves proposed that the true symmetry of maghemite is tetragonal $P4_32_12$ instead of cubic $P4_332$.[88] The lattice parameters of the tetragonal cell are $a = 8.3396$ Å and $c = 24.966$ Å, which is slightly smaller $3a$.[88] Grau-Crespo *et al.* sorted out the energetic order of various possible vacancy ordering and found that the tetragonal $P4_12_12$ configuration has much lower energy (by $\geqslant 32$ kJ mol^{-1}) than the nontetragonal configurations using classical interatomic potentials.[31] The configurations $P4_12_12$ and $P4_32_12$ bear much similarity in structure and thus should have very similar energetics. In this study, we adopted the configuration proposed by Greaves[88] (tetragonal $P4_32_12$ symmetry), each unit cell having 160 (64 Fe and 96 O) atoms. Maghemite is ferrimagnetic below Curie temperature, which is estimated to be between 820 and 960 K. The Fe atoms at the tetrahedral sites (where each Fe forms bonds with four nearest O atoms) have antiparallel spin moments with those at the octahedral sites (where each Fe forms bonds with six nearest O atoms). Specifically, the 40 Fe atoms in the 3 × 1 supercell at positions [1/8,5/8,0], [3/8,1/8,2/24], [1/8,7/8,2/24], [7/8,5/8,2/24], [3/8,3/8,0], and [7/8,7/8,0] consist of the majority spin component, and the 24 Fe atoms at [4/8,6/8,1/24], [0,2/8,1/24], and [2/8,4/8,3/24] consist of the minority spin moment. Measurements of magnetic moments (spin polarization + orbital moment) showed that Fe atoms at the octahedral and tetrahedral sites have unequal spin moments: $3.54\mu_B$ versus $4.03\mu_B$,[89] or $4.18\mu_B$ versus $4.41\mu_B$.[88] In addition to this ferrimagnetization, we include ferromagnetic and nonmagnetic states for validation of the calculation results.

For the ferrimagnetic state, the calculated lattice constants match experimental values within 1.7% (see Table VII), with the exception of results from GGA + U using LCAO, in which the errors are about 3.1%. In general, the results from PW calculations are closer to those reported from experiments. If we omit spin polarization, the lattice parameters decrease simultaneously in both calculations, and the mismatch in lattice constants between the calculations and experiments increases to −4.4%. Including on-site interaction leads to a lattice expansion of about 1% in both PW and LCAO. Both

TABLE VI. Calculated bulk moduli and elastic constants of hematite. Unit: GPa.

	PW		LCAO	
	GGA	GGA + U	GGA	GGA + U
B	174.4	190.3	173.4	176.1
c_{11}	325.0 ± 19.0	355.4 ± 13.9	310.3 ± 12.1	319.6 ± 18.6
c_{12}	131.8 ± 5.6	132.1 ± 6.4	137.2 ± 0.3	125.6 ± 4.3
c_{13}	105.8 ± 22.9	116.0 ± 4.0	114.6 ± 6.9	104.5 ± 1.5
c_{14}	1.2 ± 2.9	−5.6 ± 6.4	6.1 ± 6.9	5.5 ± 9.4
c_{33}	264.2 ± 25.1	307.2 ± 3.3	255.6 ± 3.8	294.4 ± 9.8
c_{44}	103.0 ± 6.4	110.6 ± 7.0	78.4 ± 4.9	80.1 ± 5.2

TABLE VII. Calculated thermodynamic properties of maghemite. See Table V for annotations.

		a (Å)	c (Å)	M (μ_B)	E_f (kJ mol^{-1})
PW	FiM	8.363 (+0.3)	25.034 (+0.3)	1.25	−623.9
	FoM	8.192 (−1.8)	24.563 (−1.6)	2.75	−568.9
	NM	8.026 (−3.8)	24.871 (−4.4)		−508.5
	GGA + U	8.428 (+1.1)	25.237 (+1.1)	1.25	
LCAO	FiM	8.480 (+1.7)	25.374 (+1.6)	1.25	−661.4
	FoM				
	NM	8.059 (−3.4)	24.153 (−3.3)		−496.5
	GGA + U	8.598 (+3.1)	25.718 (+3.1)	1.25	
Expt.[a]		8.34	24.97		−806 to −813

[a] Measured at room temperature and 0.1 MPa. Ref. 1, pp. 11 and 187.

calculations reproduce the correct magnetic ordering, predicting that ferrimagnetic state has a lower formation energy than nonmagnetic and ferromagnetic states. By comparing Tables VII and V, one immediately sees that maghemite has a higher formation energy, and thus is less thermodynamically stable than hematite.

In the case of maghemite, the calculated elastic properties are very similar, both in trend and numbers, when we compare the PW and LCAO calculations (see Table VIII). The diagonal components (c_{11} and c_{33}) of the elasticity tensor are noticeably larger in GGA + U than GGA; the shear moduli (c_{44} and c_{55}) are also slightly larger when using GGA + U. We find that in all the calculations, $c_{11} \approx c_{33}$, $c_{12} \approx c_{13}$, and $c_{44} \approx c_{55}$, which are conditions characteristic of the elasticity tensors of cubic crystals. This is indicative of the similarity between the tetragonal lattice of maghemite with its cubic counterpart. Although the long-range ordering of vacancies changes the symmetry of the lattice, the elasticity tensor seems to be insulated from the change of symmetry.

E. Goethite (α-FeOOH)

Goethite is the most thermodynamically stable iron oxyhydroxide, and has orthorhombic structure (space group $Pnma$, No. 62).[90] The lattice parameters have been measured by synchrotron powder diffraction at temperatures between 298 and 429 K,[90] and at pressures up to 9 GPa.[91] Gleason *et al.*[92] studied the equation of state of goethite under pressures

TABLE VIII. Calculated bulk moduli and elastic constants of maghemite. Unit: GPa.

	PW		LCAO	
	FiM	GGA + U	FiM	GGA + U
B_0	146.3	147.8	134.4	145.9
c_{11}	264.3 ± 27.0	285.0 ± 20.8	245.2 ± 12.3	266.3 ± 31.2
c_{12}	122.5 ± 16.8	120.0 ± 12.6	114.2 ± 9.0	113.2 ± 22.7
c_{13}	124.4 ± 17.9	120.1 ± 14.9	113.1 ± 1.1	114.2 ± 15.4
c_{33}	265.7 ± 10.7	284.1 ± 9.4	246.0 ± 4.3	266.7 ± 12.7
c_{44}	103.7 ± 0.2	106.0 ± 0.1	90.9 ± 2.7	94.3 ± 3.2
c_{55}	103.0 ± 0.2	106.5 ± 0.0	92.4 ± 1.8	95.8 ± 6.5

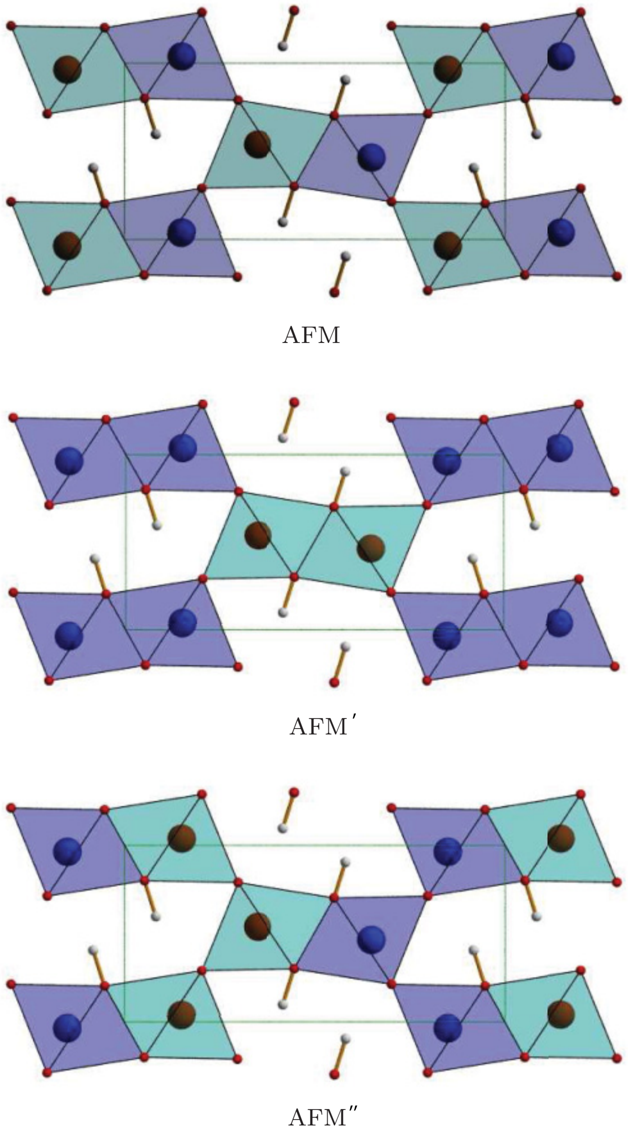

FIG. 5. (Color online) Antiferromagnetic configurations of goethite. Cyan and blue octahedrons are for Fe atoms with antiparallel spin moments. Red balls are oxygen, white balls are hydrogen, sticks are hydroxyl bonds. Viewed along the [010] direction.

0–250 GPa, and found the equilibrium volume is 138.75 ± 0.02 Å^3, bulk modulus is 140.3 ± 3.7 GPa, and pressure derivative is 4.6 ± 0.4. Goethite is antiferromagnetic in its ground state, with an edge-sharing octahedron within a double-chain having antiparallel spin moments, and a corner-sharing octahedron in two double-chains having antiparallel spin moments (see Fig. 5). In addition to this antiferromagnetic state, we included another two antiferromagnetic states; one has the same spin in a double-chain (denoted as AFM′), the other is similar to AFM except the corner-sharing octahedron has parallel spin (denoted as AFM″). We have also calculated a ferrimagnetic, a ferromagnetic, and a nonmagnetic state.

The energetic order of antiferromagnetic states is the same in both PW and LCAO calculations. The energy difference between AFM and AFM′ is only about 3 kJ mol^{-1}, which is, however, near the limits of the computation accuracy. The small energy difference between AFM and AFM′ is reproduced in both the GGA + U and GGA calculations, using both the PW and LCAO basis sets. Despite this reproducibility across different basis sets, further calculations with high accuracy are required to distinguish the energetic order of the two antiferromagnetic states. The energies of AFM and AFM′ are lower than AFM″ by about 30 kJ mol^{-1} in both PW and LCAO, indicating that the corner-sharing octahedron of antiparallel spins (as in AFM and AFM′) are energetically more stable than that of parallel spins (as in AFM″). In this study, we assume the AFM state is more energetically stable than AFM′, and perform calculations of elastic properties based on the AFM magnetization state with and without on-site interaction.

As we see from the calculation results in previous sections (hematite and maghemite), the lattice parameters from GGA + U are usually larger than that of GGA. This trend is violated in the calculation to lattice parameter c. In the PW calculations, the GGA + U result is smaller than GGA, while in the LCAO results, the calculated c are almost the same (Table IX). This feature is also seen in the calculation results of the b axis of lepidocrocite (see Sec. III F). Since the hydrogen bonds are almost along the c axis in goethite (and the b axis in lepidocrocite), the smaller values of lattice parameter c in goethite (and b in lepidocrocite) indicate strengthening of hydrogen bonds in the GGA + U calculations compared with the GGA calculations. The physical origin of this observation is not clear yet. Possible explanations may be from the redistribution of the charge density caused by the on-site Coulomb interactions. Although Fe atoms are not part of the hydrogen bonds (H-O ··· H), they have an influence on the strength of hydrogen bonds by modifying the electron density in Fe-O bonds, which (in turn) change the electron density around the oxygen atoms, which are acceptors of the hydrogen bonds. The on-site Coulomb repulsion among Fe 3d electrons decreases the charge density in Fe-O bonds, increasing the electron density around the oxygen atoms and strengthening the hydrogen bonds. The changes in electron density will be illustrated in more detail in a separate paper.

The ferrimagnetic state has the same average spin polarization moment in both calculations. Like the results of hematite, the spin moment of the ferromagnetic state is quite different: low spin in PW and high spin in LCAO. With the exception of this difference in spin moments of the ferromagnetic state, the calculation results from the PW and LCAO basis sets are consistent with each other.

The calculated bulk moduli and elastic constants of the AFM state are listed in Table X. We found that GGA + U calculations produce appreciably larger values of bulk moduli and most tensor components than the GGA in both PW and LCAO basis sets. The reason for the strengthening effect of GGA + U is not clear. It may be related to the hydrogen bonds, which are sensitive to the distribution of electron density, but further work will be needed to understand this definitively.

F. Lepidocrocite (γ-FeOOH)

Lepidocrocite has an orthorhombic structure [space group $Cmc2_1$, No. 36 (Ref. 93)], which consists of double chains

TABLE IX. Calculated thermodynamic properties of goethite. See Table V for annotations.

		a (Å)	b (Å)	c (Å)	M (μ_B)	E_f (kJ mol^{-1})
PW	AFM	10.018 (+0.6)	3.017 (−0.1)	4.661 (+1.2)	0.00	−453.1
	AFM′	10.025 (+0.7)	3.015 (−0.2)	4.650 (+0.9)	0.00	−450.4
	AFM″	10.045 (+0.9)	3.055 (+1.1)	4.655 (+1.0)	0.00	−419.6
	FiM	10.039 (+0.8)	3.042 (+0.7)	4.664 (+1.2)	2.50	−432.9
	FoM	10.103 (+1.5)	2.842 (−5.9)	4.560 (−1.0)	2.63	−417.6
	NM	9.529 (−4.3)	2.920 (−3.3)	4.366 (−5.2)		−415.6
	GGA + U	10.040 (+0.8)	3.045 (+0.8)	4.628 (+0.4)	0.00	
LCAO	AFM	10.148 (+1.9)	3.060 (+1.3)	4.654 (+1.0)	0.00	−492.9
	AFM′	10.149 (+1.9)	3.061 (+1.3)	4.656 (+1.0)	0.00	−490.0
	AFM″	10.171 (+2.2)	3.092 (+2.3)	4.683 (+1.6)	0.00	−463.7
	FiM	10.177 (+2.2)	3.079 (+1.9)	4.673 (+1.4)	2.50	−475.2
	FoM	10.200 (+2.4)	3.100 (+2.6)	4.695 (+1.9)	4.99	−456.6
	NM	9.642 (−3.2)	2.939 (−2.7)	4.353 (−5.5)		−428.4
	GGA + U	10.207 (+2.5)	3.105 (+2.8)	4.663 (+1.2)	0.00	
Expt.[a]		9.956	3.021	4.608	0.00	−559.3, −562.9

[a] Measured at room temperature and 0.1 MPa. Ref. 1, pp. 11 and 187.

TABLE X. Calculated bulk moduli and elastic constants of goethite. Unit: GPa.

	PW		LCAO	
	AFM	GGA + U	AFM	GGA + U
B_0	93.1	114.1	98.6	109.4
c_{11}	235.4 ± 3.8	298.4 ± 4.4	231.7 ± 8.4	252.2 ± 5.3
c_{12}	89.0 ± 1.2	106.2 ± 4.8	86.6 ± 5.4	89.2 ± 0.4
c_{13}	112.2 ± 5.2	117.4 ± 3.6	111.4 ± 8.5	117.7 ± 6.0
c_{22}	263.8 ± 4.3	347.9 ± 3.6	234.0 ± 10.0	271.7 ± 1.4
c_{23}	96.3 ± 6.1	105.7 ± 2.0	87.3 ± 11.1	99.0 ± 1.7
c_{33}	406.7 ± 6.5	414.8 ± 3.9	363.3 ± 12.0	369.2 ± 5.1
c_{44}	78.9 ± 0.1	105.0 ± 0.3	58.7 ± 0.2	91.0 ± 0.4
c_{55}	122.6 ± 0.7	131.4 ± 0.0	106.9 ± 2.8	122.4 ± 2.1
c_{66}	65.9 ± 0.0	97.3 ± 0.6	60.1 ± 2.1	72.3 ± 4.8

of an Fe(O,OH)$_6$ octahedron that are aligned perpendicular to the b axis. The double chains form sheets, held together mainly by hydrogen bonds, which are weaker than covalent or metallic bonds, and may be longer than normal chemical bonds. Depending on the position of hydrogen atoms, the crystal structure of lepidocrocite can either be in the $Cmcm$ space group (No. 63), where the hydrogen atom resides at the middle of two oxygen atoms in a hydrogen bond,[94,95] or in the $Cmc2_1$ space group (No. 36), where the hydrogen atom is closer to one of the two oxygen atoms.[93] The difference is that $Cmc2_1$ is noncentrosymmetric, but is indistinguishable from the centrosymmetric $Cmcm$ in XRD or neutron diffraction. The bond distances in the H bonds in the $Cmcm$ space group are extraordinarily large, thus the positions of hydrogen atoms may be averaged positions in neutron diffraction,[95] and the true symmetry may be $Cmc2_1$ (which has normal bond distances). We adopted the proposal in Ref. 93 as the starting structure for our calculations.

Each primitive cell contains two iron atoms, whose spin moment may align in parallel (ferromagnetic) or antiparallel (antiferromagnetic) configurations. More magnetization states may be included if the magnetization state is stated in a conventional cell that contains four iron atoms. Lepidocrocite is antiferromagnetic with antiparallel spins in the same double layer and antiparallel spins linked by hydrogen bonds.[93] This antiferromagnetic state is denoted as AFM in this paper (Fig. 6). Another two antiferromagnetic states, denoted AFM$'$ and AFM$''$, are also included for comparison in addition to one ferrimagnetic, one ferromagnetic, and one nonmagnetic state. AFM$'$ is similar to AFM, except the octahedron linked by hydrogen bonds has parallel spin moments; AFM$''$ has parallel spin in a double layer and antiparallel spin in neighboring double layers.

The calculated thermodynamic properties of lepidocrocite are listed in Table XI, where we can see that calculations performed using the LCAO basis set produce larger error with respect to available experimental values than those obtained from the PW calculations. The largest error in our LCAO calculations is the overestimation of the lattice parameter c by about 7.6%. The magnetization state of AFM$'$ also deviated from antiferromagnetic, and converged to a ferrimagnetic state during geometry optimization in LCAO calculations. The nonmagnetic state has larger errors in both calculations than other states, which is consistent with the results obtained for the other iron oxides and oxyhydroxides, as described in previous sections.

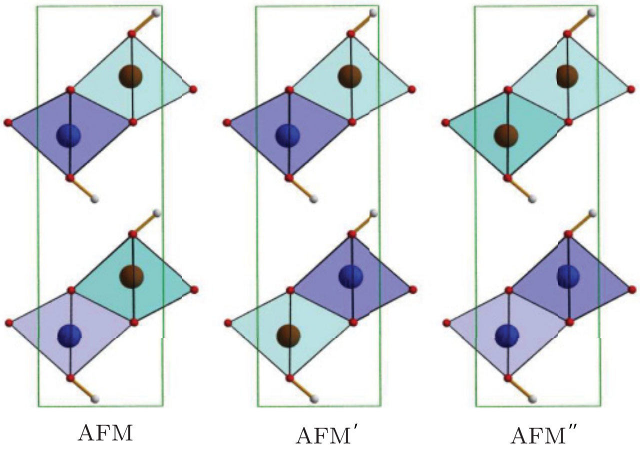

FIG. 6. (Color online) Three antiferromagnetic configurations of lepidocrocite. Cyan and blue octahedrons are for Fe atoms with antiparallel spin moments. Red balls are oxygen, white balls are hydrogen, sticks are hydroxyl bonds. Viewed along the [010] direction.

In this case, the energetic order predicted by PW and LCAO calculations compares very well among all the magnetization states, with the exception of the AFM$'$ state (which deviates from the initial antiferromagnetic state) in LCAO calculations. The energy difference between the AFM and AFM$''$ states is almost the same, about 10 kJ mol^{-1}, using both PW and LCAO. This indicates that the spin moments in a double layer are unlikely to be parallel, as in the energetically unstable AFM$''$. The AFM$''$ and FoM states have almost the same formation energies in both calculations, indicating there is weak correlation between iron atoms connected by hydrogen bonds. This can also be seen from a comparison of the AFM and AFM$'$ states, between which the difference is solely due to the alignment of spin moments of iron atoms linked by hydrogen bonds. The formation energies of lepidocrocite (Table XI) are higher than those of goethite (Table IX), which is in good agreement with the established thermodynamic stability of the two iron oxyhydroxide phases (where goethite is known to be more stable than lepidocrocite).

At this point, we would like to highlight that a correct description of the loose, layered structure of lepidocrocite is much more difficult to obtain in our computations (using both PW and LCAO basis sets) than other types of oxides and oxyhydroxides. Geometry optimizations often become trapped in an incorrect structure, as shown in Fig. 7. In the incorrectly optimized structure, the iron atoms are trigonal-bipyramid coordinated instead of octahedron, while the oxygen atoms that do not form hydroxyl bonds are bonded to only three iron atoms instead of four. The incorrect structure may have an abnormally small lattice parameter a (up to about 20% below experimental value), large b (up to about 25% above experimental value), or large c (up to about 40% above experimental value). These incorrect structures occurred when the geometry optimizations began using the structure models that have hydrogen atoms equidistant between oxygen atoms,

TABLE XI. Calculated thermodynamic properties of lepidocrocite. See Table V for annotations.

		a (Å)	b (Å)	c (Å)	M (μ_B)	E_f (kJ mol^{-1})
PW	AFM	3.038 (−1.4)	12.624 (+1.0)	3.896 (+0.7)	0.00	−425.8
	AFM′	3.046 (−1.1)	12.604 (+0.8)	3.908 (+1.0)	0.00	−425.2
	AFM″	3.080 (+0.0)	12.204 (−2.4)	3.866 (−0.1)	0.00	−417.4
	FiM	3.066 (−0.4)	12.390 (−0.9)	3.898 (+0.7)	2.03	−421.9
	FoM	3.086 (+0.2)	12.233 (−2.1)	3.862 (−0.2)	4.17	−416.9
	NM	2.900 (−5.9)	11.846 (−5.2)	3.795 (−1.9)		−398.2
	GGA + U	3.074 (−0.2)	12.546 (+0.4)	3.935 (+1.7)	0.00	
LCAO	AFM	3.061 (−0.6)	12.417 (−0.7)	4.165 (+7.6)	0.00	−463.5
	AFM′	3.107 (+0.9)	12.533 (+0.3)	4.029 (+4.1)	2.47	−457.8
	AFM″	3.125 (+1.5)	12.456 (−0.4)	4.021 (+3.9)	0.00	−452.7
	FiM	3.107 (+0.9)	12.532 (+0.3)	4.029 (+4.1)	2.48	−457.8
	FoM	3.128 (+1.5)	12.472 (−0.2)	4.021 (+3.9)	4.94	−452.0
	NM	2.912 (−5.5)	11.745 (−6.0)	3.853 (−0.4)		−406.5
	GGA + U	3.091 (+0.4)	12.487 (−0.1)	4.011 (+3.6)	0.00	
Expt.[a]		3.08	12.50	3.87	0.00	−554.6

[a] Measured at room temperature and 0.1 MPa. Ref. 1, pp. 11 and 187.

and may also occur with certain computational settings. We show the equation of state (EOS) calculated using GGA and GGA + U to demonstrate the sensitivity of geometry optimization by GGA on the starting structure (Fig. 8). The incorrect structure is accompanied by the steep energy decrease when the cell volume is slightly larger (3%; the correct structure can retain up to 1% volume increase) than the equilibrium volume. In contrast, the GGA + U is robust in geometry optimizations with varying volume in this case. We carefully examined the final structures after geometry optimization, and rigorously tested the computational settings and initial structures to ensure the double-layer structure of lepidocrocite.

In the case of lepidocrocite, the calculation results of elastic properties are more diverged than for other iron oxides and oxyhydroxides in this paper. As shown in Table XII, the difference between GGA and GGA + U can be more than 50% (c_{13}, c_{22}, and c_{66} in PW; c_{55} and c_{66} in LCAO), and the agreements between PW and LCAO are acceptable only for components c_{22}, c_{23}, and c_{33}. This is partly due to the delicacy of lepidocrocite.

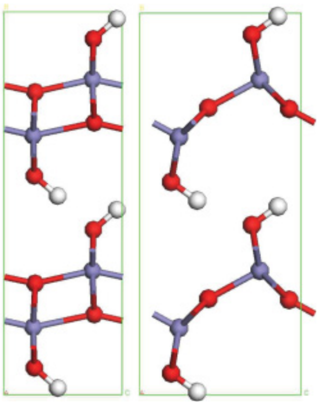
Correct Incorrect

FIG. 7. (Color online) Structural abnormality in geometry optimization. Gray blue balls are Fe, red are O, and white are hydrogen. Viewed along the [010] direction.

G. Magnetite (Fe_3O_4)

Magnetite has a cubic inverse spinel structure (space group $Fd\bar{3}m$, No. 227) at thermodynamic standard state (room temperature, ambient pressure). Its chemical formula, Fe_3O_4, is often written as $Fe^{3+}[Fe^{3+},Fe^{2+}]O_4$ to show that tetrahedral sites (A) are occupied by trivalent Fe ions, and octahedral sites (B) are occupied by equal trivalent and divalent ions. The spin moments of A and B sites align antiparallel, resulting in a ferrimagnetic state. Magnetite undergoes the Verwey phase transition at about 125 K, below which the electronic resistivity increases by two orders of magnitude.[96] This phenomenon was explained by a charge-ordering model in which electron hopping among Fe ions is frozen below the Verwey transition temperature and aligned in an ordered pattern.[96] However, after six decades of study, researchers

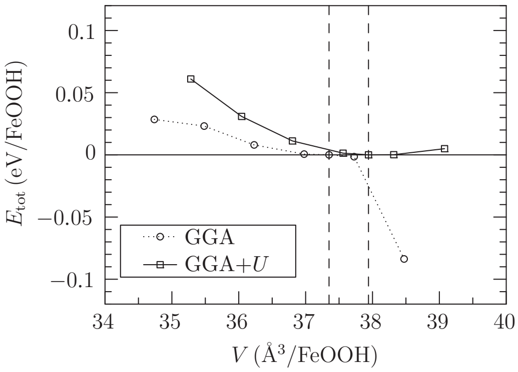

FIG. 8. Equation of state of lepidocrocite in GGA and GGA + U calculations, both using the PW basis set. The two vertical dashed lines mark the equilibrium volumes optimized by GGA and GGA + U. The total energies are shifted to align the minimum energies of GGA and GGA + U.

TABLE XII. Calculated bulk moduli and elastic constants of lepidocrocite. Unit: GPa.

	PW		LCAO	
	AFM	GGA + U	AFM	GGA + U
B_0	75.6	74.8	x	81.8
c_{11}	219.0 ± 22.8	246.9 ± 9.8	242.4 ± 0.9	264.5 ± 12.8
c_{12}	77.3 ± 14.5	84.8 ± 6.8	88.0 ± 0.2	95.1 ± 13.2
c_{13}	31.9 ± 26.8	80.6 ± 10.1	79.0 ± 1.2	72.2 ± 3.8
c_{22}	221.0 ± 11.6	272.2 ± 18.7	214.7 ± 1.7	246.3 ± 10.4
c_{23}	123.3 ± 8.5	137.2 ± 22.9	127.3 ± 0.9	124.1 ± 4.9
c_{33}	305.4 ± 21.9	347.7 ± 16.8	303.2 ± 1.6	327.4 ± 4.5
c_{44}	121.6 ± 0.0	131.4 ± 0.0	97.6 ± 1.2	119.0 ± 0.8
c_{55}	63.4 ± 0.0	64.0 ± 0.1	49.2 ± 0.8	63.6 ± 1.9
c_{66}	44.8 ± 0.0	88.9 ± 0.1	73.3 ± 0.6	93.6 ± 1.5

found that the phenomenon is far more complicated than was previously thought.[97] Among various changes (electronic resistivity, band structure, heat capacity) accompanied by the Verwey transition, the structure distorted slightly from the room-temperature cubic structure. At low temperatures, the structure of magnetite was proposed to be orthorhombic from nuclear magnetic resonance spectroscopy;[98–100] monoclinic from x-ray diffraction,[14,101] neutron diffraction,[15] electron diffraction,[16] and x-ray resonant scattering;[102] or even lower symmetry of triclinic.[103] In the present study, we have restricted our calculation to the room-temperature cubic structure because the calculated thermodynamic properties at ground state can be extrapolated to room temperature without discontinuity by the phase transition.

In the case of magnetite, we have tested three magnetization states: FiM, FoM, and NM. Both PW and LCAO basis sets predict that the FiM state has the lowest formation enthalpy among all these magnetization states (see Table XIII). The lattice constants of the FiM state also provide better agreement with the experimental measurements. Using both basis sets, the calculation results differ from experimental values if we ignore spin polarization. The error in lattice constants using the LCAO approach is slightly larger than that using the PW approach. The calculated spin moments agree well with each other in both PW- and LCAO-based methods.

TABLE XIII. Calculated thermodynamic properties of magnetite. See Table V for annotations.

		a (Å)	M (μ_B)	E_f (kJ mol^{-1})
PW	FiM	8.392 (−0.0)	1.33	−871.7
	FoM	8.528 (+1.6)	4.57	−747.1
	NM	8.049 (−4.1)		−666.4
	GGA + U	8.481 (+1.0)	1.33	
LCAO	FiM	8.504 (+1.3)	1.33	−930.9
	FoM	8.645 (+3.0)	4.67	−828.7
	NM	8.111 (−3.3)		−650.2
	GGA + U	8.653 (+3.1)	1.33	
Expt.[a]		8.396		∼ − 1120

[a] Measured at room temperature and 0.1 MPa. Ref. 1, pp. 11 and 187.

TABLE XIV. Calculated bulk moduli and elastic constants of magnetite. Unit: GPa. The calculation results with GGA + U are discussed in the main text.

	PW		LCAO	
	FiM	GGA + U	FiM	GGA + U
B	187.4	173.3	165.3	168.3
c_{11}	275.4 ± 40.9		253.6 ± 5.7	
c_{12}	155.2 ± 60.3		128.1 ± 10.3	
c_{44}	97.5 ± 13.0		75.4 ± 0.9	

We calculated the elastic properties (bulk moduli and elasticity tensor) of FiM magnetite, as shown in Table XIV. GGA calculations using PW and LCAO both predict that cubic magnetite is elastically stable. In the case of GGA + U calculations, we were unable to fit the strain energies with strains to calculate elastic constants, because the equilibrium cubic structure has higher energy than strained states. As shown in Fig. 9, except for the isotropic deformation, the other two deformations have even lower energy than the zero-strain "equilibrium" structure in GGA + U calculations. Increasing the k-point sampling density does not solve this problem. This indicates that the cubic magnetite is elastically unstable, which agrees well with experimental observations that the low-temperature (below Verwey transition temperature) structure is monoclinic, but not cubic.

H. Energetic order

As mentioned above, one of the computational challenges in modeling different iron oxides and oxyhydroxides is the small energy differences among different solid phases. Since the typical accuracy of DFT calculations is about several kJ mol^{-1}, which is comparable to the energy differences between competing phases, calculations with different settings may lead to very different energetic order, but may have very little physical meaning due to numerical inconsistencies. Systematic and consistent calculations of all the phases are highly desirable to make comparisons among the different phases, as well as case-by-case comparisons with experiments. The calculations in this study have enabled us to assess the PW

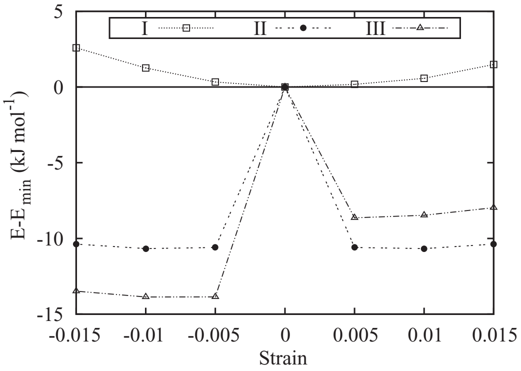

FIG. 9. Strain energies in calculations to elastic constants of GGA + U using PW. The three deformations are I (isotropic) $\begin{pmatrix} 1 & 0 & 0 \\ 0 & 1 & 0 \\ 0 & 0 & 1 \end{pmatrix}$, II (orthorhombic) $\begin{pmatrix} 1 & 0 & 0 \\ 0 & -1 & 0 \\ 0 & 0 & 0 \end{pmatrix}$, and III (shear) $\begin{pmatrix} 0 & 1/2 & 1/2 \\ 0 & 0 & 1/2 \\ 1/2 & 1/2 & 0 \end{pmatrix}$.

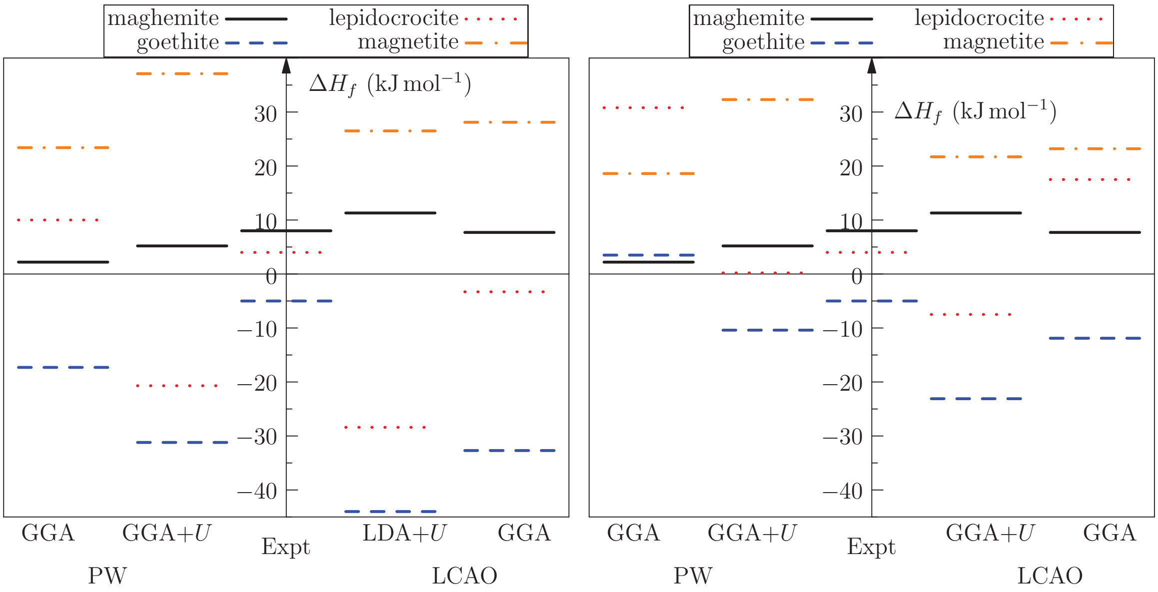

FIG. 10. (Color online) Calculated formation enthalpies of iron oxides and oxyhydroxides with respect to hematite and water or oxygen without (left) and with (right) corrections of connection energies. The formation enthalpies of goethite and lepidocrocite are with respect to hematite and water; magnetite is with respect to hematite and oxygen. Expt stands for experimental values. All the enthalpies are normalized to per mole of Fe.

and LCAO basis sets, but also to make such comparisons for the first time.

To begin with, we have calculated the formation enthalpies of the iron oxides and oxyhydroxides with respect to hematite and water or oxygen (Fig. 10). Available experimental values[104] are also shown in the figure for comparison. Among the five iron oxides and oxyhydroxides, magnetite is typically excluded from the experiments because all the other four compounds (goethite, lepidocrocite, maghemite, and hematite) can be rewritten as hematite $+ x\mathrm{H_2O} + \Delta H_f$ ($x = 0$ for maghemite or 0.5 for goethite and lepidocrocite). In our work, we are able to include magnetite and compare the energetic order with respect to hematite and oxygen. In this way, we can plot the energetic order of all five iron oxides and oxyhydroxides together, keeping hematite plus balancing gases ($\mathrm{H_2O}$ and $\mathrm{O_2}$ in their standard state) as the reference.

At this point, it is prudent to point out that our DFT calculations correspond to the ground state, while experiments were conducted at the thermodynamic standard state. The influence of temperature and pressure on the formation energies of solids is much less than that of gases. We therefore include the connection energy, which defines the difference between energies at ground state and standard state, for the gases.[105] By this *ab initio* thermodynamics scheme, we can extend the calculation results at ground state to finite temperature and pressures. In this case, we use the connection energies for the gases, which have been calculated to solve tribochemistry problems.[106] For solids, the available thermochemistry data enable one to calculate connection energy by integrating from the 0 K ground state to the thermodynamic standard state as

$$\Delta\mu^0(T_r) = \int_{0\,\mathrm{K}}^{T_r} C_p dT - T\int_{0\,\mathrm{K}}^{T_r} \frac{C_p}{T} dT, \qquad (2)$$

where $\Delta\mu^0(T_r)$ is the connection energy at standard pressure ($p^0 = 1$ atm) and room temperature $T_r = 298.15$ K, and C_p is the molar heat capacity. The heat capacity, enthalpy difference between room temperature and 0 K, and entropy can be looked up in thermochemistry tables, for example, the NIST-JANAF table.[107] Calculations of the connection energies of gases are usually done through reaction equilibrium with solids. For example, we used the reaction

$$\mathrm{MgO} + \mathrm{H_2O} \leftrightarrow \mathrm{Mg(OH)_2} \qquad (3)$$

to calculate the connection energy of gas-phase water because the thermochemical data of MgO and $\mathrm{Mg(OH)_2}$ are available.[106] Once the connection energies for room temperature are known, the chemical potentials at other temperatures (and pressures for gases) can be readily calculated using thermodynamics as long as the heat capacity data are available for the temperature range.

From Fig. 10, we see that the enthalpy difference between maghemite and hematite is apparently underestimated (by about 5 kJ mol^{-1}) when using GGA with the PW basis set, while all other settings reproduce this energy difference well. For magnetite, the enthalpy calculated using GGA + U with PW is larger than others, but the energetic order is consistent in all the calculations. The energy difference between goethite and lepidocrocite is larger in GGA than that in GGA + U, in both PW and LCAO calculations. It is worth noting that the corrections using connection energy are ineffective to change the relative energetic orders of hematite and maghemite, or goethite and lepidocrocite, because they have the same chemical compositions. However, with the corrections of connection energies, the relative energetic order between compounds with different composition may change, as we see in the subfigures in Fig. 10. With the corrections, the difference between the state for calculations and experiments is approximately eliminated, enabling us to make fair comparisons. The calculated energetic order of lepidocrocite, hematite, and maghemite is

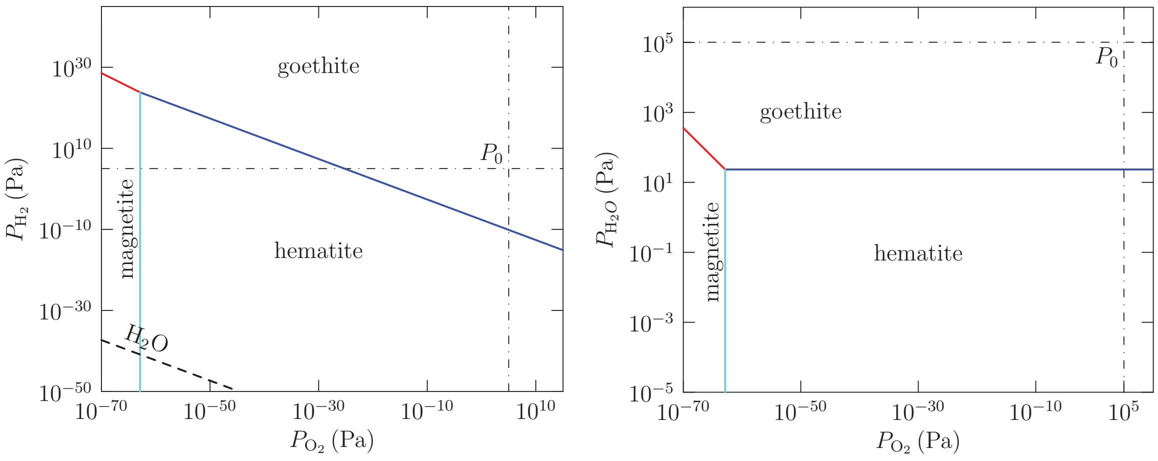

(a) (b)

FIG. 11. (Color online) Phase diagram of iron oxides and oxyhydroxides with partial pressures of gases at $T = 298.15$ K. Lepidocrocite is metastable with respect to goethite, and maghemite is metastable to hematite; they are excluded in this equilibrium phase diagram. Dash-dotted lines indicate standard pressure (1 atm); the dashed line in (a) indicates the formation of water vapor from H_2 and O_2 with no energy gain or loss. Note the different scales of partial pressures of H_2 in (a) and H_2O in (b).

very different in the four data sets, and we may conclude that GGA + U with PW implementation best matches experiment.

The consistent computational settings across different iron oxides and oxyhydroxides offer us a number of significant advantages, one of which is that we are in a position to construct phase diagrams. For this purpose, we have chosen to use the calculation results from GGA + U with the PW implementation, and compute the free energy of formation of a compound FeO_xH_y as

$$\Delta G = \Delta H - \frac{x}{2}\left(\Delta_{O_2}(T) + RT \ln \frac{P_{O_2}}{P^0}\right) - \frac{y}{2}\left(\Delta_{H_2}(T) + RT \ln \frac{P_{H_2}}{P^0}\right), \quad (4)$$

where ΔH is the formation energy at ground state, $\Delta_{O_2}(T)$ and $\Delta_{H_2}(T)$ are connection energies at a certain temperature for O_2 and H_2, respectively, and R is the gas constant. One can write the formation energies with respect to H_2O and O_2 by analogy. The connection energies were calculated using thermochemistry data in a previous study,[106] and ΔH are from the ground-state calculations in the present study. In a phase diagram, the phase boundaries determined from Eq. (4) are straight lines in a phase diagram.

Using Eq. (4), we have constructed two phase diagrams, both corresponding to room temperature (see Fig. 11). The metastable phases of lepidocrocite and maghemite are not shown, as these are equilibrium phase diagrams. The two subfigures refer to the same systems with respect to the chemical potentials of (a) H_2 and O_2 and (b) H_2O and O_2, respectively. One notices the extremely low partial pressure of oxygen required for the formation of magnetite instead of hematite. This means that, at room temperature, magnetite should form under oxygen-poor conditions; otherwise the more stable hematite phase should prevail in oxygenous environments. This is compatible with the fact that most magnetotactic bacteria that produce magnetite are either anaerobic or microaerobic[1] (pp. 481–489). Magnetite is able to form from hematite at low temperatures in the presence of hydrazine[1] (pp. 405 and 406), which removes dissolved oxygen in the solutions.

The phase boundary between hematite and goethite has the same slope of water formation in Fig. 11(a); therefore, in a phase diagram of Fe-H_2O-O_2, it is independent of chemical potential of H_2O, as shown in Fig. 11(b). The phase diagram shows that the free energy of goethite is lower than hematite at standard state, and this agrees with the calorimetry measurements.[104] In a wet environment, these phase diagrams predict that the formation of goethite will be more thermodynamically favorable than hematite; while dehydration (dry conditions) will cause goethite to transform into hematite given a suitable driving force.

IV. COMPARISON OF EFFICIENCY

One of the advantages of LCAO basis sets is efficiency.[32,36,37,47] The atomic orbitals used to expand the wave functions are very economic (in terms of number of orbitals per atom to achieve accuracy) compared with the PW basis set. In the DZP scheme that is used in the present study, each Fe atom needs 17 orbitals for the valence electrons, O needs 13, and H needs 3. For a 4 × 4 × 4 k-point grid for hematite, the number of atomic orbitals is 8832. To achieve similar convergence in energy calculations, the PW basis set requires about 120 000 PW's, which is about 15 times that of the LCAO basis set. The advantage of fewer orbitals will be even more apparent if the computation cell has vacuum space, such as in surface calculations, since the LCAO's are centered at ions, and vacuum requires no additional orbitals. In contrast, the PW's are delocalized, and even vacuum space has a similar number density of PW's.

In addition, the localized nature of LCAO's enables one to implement the order-N algorithms, which critically rely on the localization of wave functions. In integrating over bands, the Fermi level needs to reside in the band gap, which should be

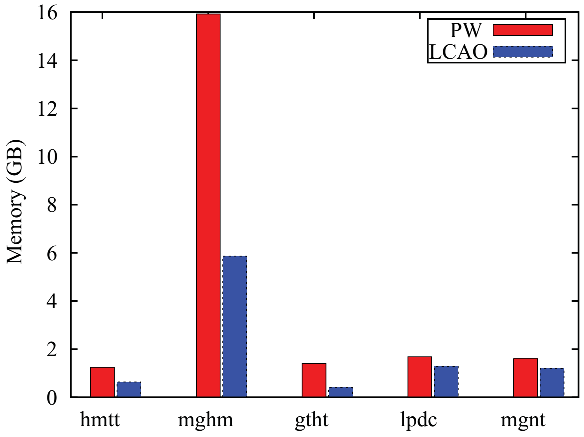

FIG. 12. (Color online) Memory requirement of PW and LCAO in geometry optimizations to the iron oxides.

large enough to cover the varying chemical potential. This is not true for metals and semiconductors with narrow band gaps, which include most iron oxides and oxyhydroxides. Therefore, studies on these systems are not able to benefit from the order-N algorithms.

However, fewer orbitals should still translate into efficiency (of computation time and memory usage), even without order-N algorithms. We find this is true for memory usage, but it is not always true for computation time. As shown in Fig. 12, the PW basis set uses more memory than LCAO for calculations of all the iron oxides and oxyhydroxides included in our study. It is worth noting that the memory requirements also depend on parallelization, and the numbers are extracted from calculations using eight CPU's for all the iron oxides except maghemite, which uses 32 CPU's. The CPU time usage for geometry optimizations for different magnetization states of hematite (Fig. 13) shows that the PW basis set may exceed LCAO in some geometry optimizations, even though the PW basis set uses many more orbitals. Other factors may affect the computation time, such as minimization path, so we have taken care to always start from the same structures, and use the same method (CG) and force convergence (0.005 eV/Å) in moving atoms to minimize this effect. The PW and LCAO basis sets also differ in their use of symmetry (as described above), which leads to differences in the force calculations. In general, we find that the difference in computation time is not as large as the difference in the number of orbitals. As an aside, we also compared the numbers of self-consistency iterations to reach the geometry optimization criteria. In most cases, the LCAO basis set needs more MD steps than the PW basis set to reach the convergence criteria.

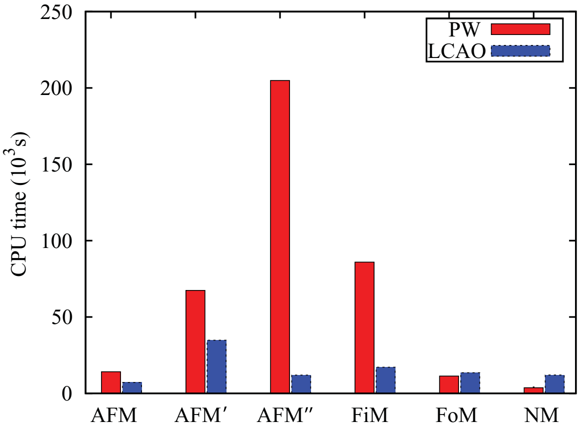

FIG. 13. (Color online) CPU time consumption in geometry optimizations to hematite.

At this point, it is also worth pointing out that one of the problems with LCAO's is systematic convergence. Simply increasing the radii of the atomic orbitals does not always lead to better convergence, and tuning the parameters of the atomic orbitals requires considerably more effort than is needed for the PW basis set. While increasing the number of atomic orbitals can increase the accuracy, this comes at the cost of computation (in the PW basis set as well). Tests of the size of atomic orbitals have shown that high accuracy within the framework of DFT can be achieved with multiple-ζ and multiple polarization orbitals. DZP, which is used in the present study, is usually a reasonable compromise between accuracy and efficiency.

V. CONCLUSIONS AND DISCUSSIONS

In summary, by comparing the calculation results of PW and LCAO basis sets, with and without on-site interactions, as well as among different magnetization configurations, we presented solutions to the computational challenge in modeling iron oxides. Consistency is paramount, and this has been maintained in the comparisons as to energy functionals, convergence criteria of force, k-point mesh, and starting structures for geometry optimizations. We have shown that both PW and LCAO basis sets can find the thermodynamically stable magnetization states, and reproduce lattice parameters well (except lepidocrocite by LCAO, which overestimates c by about 7% in GGA and 4% in GGA + U). However, in most geometry optimizations, the LCAO basis set is more efficient in CPU time and memory usage than the PW basis set, but the accuracy is slightly reduced when comparing with PW basis set. Several factors contribute to the efficiency difference between the two implementations, including number of orbitals, molecular-dynamics algorithms in moving ions, electron density mixing, force calculation, and k-point density. Using these basis sets, we evaluated the elastic stability of all the materials. We find that the PW and LCAO basis sets are comparable for most structures except lepidocrocite, and that the elasticity tensor of maghemite is close to that of a cubic crystal, though the true symmetry is tetragonal due to the long-range ordering of vacancies. While GGA predicts that cubic magnetite is elastically stable, GGA + U calculations contradict the prediction.

The crystal structure of lepidocrocite consists of layers held by H bonds. In computational modeling, functionals with GGA and hybrid functionals are able to describe the relatively weak interactions of hydrogen bonds. While van der Waals interactions may also contribute significantly to interlayer interactions, as they do in graphite, they are not included in the present study, as calculations of dispersive forces are either very expensive or rely on empirical parameters. In our calculations, this delicate structure exhibited some structural abnormalities, which may be due to the omission of dispersive forces. This layered structure is not as delicate as that of graphite (in which the carbon layers are held by even weaker van der Waals interaction), but still imposes a challenge to computational modeling. Accurate energy functionals that include van der Waals interactions may describe better the crystal structure of lepidocrocite.

Based on these results (which represent the first consistent set of *ab initio* predictions of the elastic, magnetic, and thermodynamic properties), we also present the first phase diagram of five iron oxides and oxyhydroxides designed to predict the relative stability of these materials under different chemical conditions. Given that chemical conditions are typically characteristic of specific environments (both during and after formation), this phase diagram will be invaluable in understanding the environmental stability of these important materials, and anticipating transformations that may be invoked by moving from one environment to another, or by variations in climatic conditions.

ACKNOWLEDGMENTS

The authors thank H. F. Xu and J. D. Gale for fruitful discussions on iron oxides and DFT modeling using LCAO. The authors acknowledge NCI National Facility for computational support of project code p00.

---

[1] R. M. Cornell and U. Schwertmann, *The Iron Oxides*, 2nd ed. (Wiley-VCH, Weinheim, Germany, 2003).

[2] A. Navrotsky, L. Mazeina, and J. Majzlan, Science **319**, 1635 (2008).

[3] D. S. McKay, E. K. Gibson, K. L. Thomas-Keprta, H. Vali, C. S. Romanek, S. J. Clemett, X. D. F. Chiller, C. R. Maechling, and R. N. Zare, Science **273**, 924 (1996).

[4] K. L. Thomas-Keprta, D. A. Bazylinski, J. L. Kirschvink, S. J. Clemett, D. S. McKay, S. J. Wentworth, H. Vali, E. K. Gibson, and C. S. Romanek, Geochim. Cosmochim. Acta **64**, 4049 (2000).

[5] K. L. Thomas-Keprta, S. J. Clemett, D. A. Bazylinski, J. L. Kirschvink, D. S. McKay, S. J. Wentworth, H. Vali, E. K. Gibson, M. F. McKay, and C. S. Romanek, Proc. Natl. Acad. Sci. **98**, 2164 (2001).

[6] E. K. Gibson, D. S. McKay, K. L. Thomas-Keprta, S. J. Wentworth, F. Westall, A. Steele, C. S. Romanek, M. S. Bell, and J. Toporski, Precambrian Res. **106**, 15 (2001).

[7] P. R. Buseck, R. E. Dunin-Borkowski, B. Devouard, R. B. Frankel, M. R. McCartney, P. A. Midgley, M. Rosfai, and M. Weyland, Proc. Natl. Acad. Sci. USA **98**, 13490 (2001).

[8] D. C. Golden, D. W. Ming, R. V. Morris, A. J. Brearley, H. V. Lauer Jr., A. H. Treiman, M. E. Zolensky, C. S. Schwandt, G. E. Lofgren, and G. A. McKay, Am. Mineral. **89**, 681 (2004).

[9] B. Arató, Z. Szányi, C. Flies, D. Schüler, R. B. Frankel, P. Buseck, and M. Pósfai, Am. Mineral. **90**, 1233 (2005).

[10] D. Faivre and P. Zuddas, Earth Planet. Sci. Lett. **243**, 53 (2006).

[11] W. Kohn and L. J. Sham, Phys. Rev. **140**, A1133 (1965).

[12] V. I. Anisimov, J. Zaanen, and O. K. Andersen, Phys. Rev. B **44**, 943 (1991).

[13] J. R. Cullen and E. Callen, Le Journal de Physica Colloques **32**, c1-1110 (1971).

[14] J. Yoshida and S. Iida, J. Phys. Soc. Jpn. **42**, 230 (1977).

[15] M. Iizumi, T. F. Koetzle, G. Shirane, S. Chikazumi, M. Matsui, and S. Todo, Acta Crystallogr. B **38**, 2121 (1982).

[16] J. M. Zuo, J. C. H. Spence, and W. Petuskey, Phys. Rev. B **42**, 8451 (1990).

[17] Z. Zhang and S. Satpathy, Phys. Rev. B **44**, 13319 (1991).

[18] G. K. H. Madsen and P. Novák, Europhys. Lett. **69**, 777 (2005).

[19] J. Mazo-Zuluaga and J. Restrepo, Phys. Status Solidi **2**, 3540 (2005).

[20] M. P. J. Punkkinen, K. Kokko, W. Hergert, and I. J. Väyrynen, J. Phys. Condens. Matter **11**, 2341 (1999).

[21] K. M. Rosso and J. R. Rustad, Am. Mineral. **86**, 312 (2001).

[22] G. Rollmann, A. Rohrbach, P. Entel, and J. Hafner, Phys. Rev. B **69**, 165107 (2004).

[23] I. Chamritski and G. Burns, J. Phys. Chem. B **109**, 4965 (2005).

[24] H. Shiroishi, T. Oda, I. Hamada, and N. Fujima, Polyhedron **24**, 2472 (2005).

[25] J. D. Kubicki, K. W. Pau, and D. L. Sparks, Geochem. Trans. **9**, 4 (2008).

[26] R. Pentcheva, W. Moritz, J. Rundgren, S. Frank, D. Schrupp, and M. Scheffler, Surf. Sci. **602**, 1299 (2008).

[27] G. J. Martin, R. S. Cutting, D. J. Vaughan, and M. C. Warren, Am. Mineral. **94**, 1341 (2009).

[28] N. Pinney, J. D. Kubicki, D. S. Middlemiss, C. P. Grey, and D. Morgan, Chem. Mater. **21**, 5727 (2009).

[29] B. Russell, M. Payne, and L. C. Ciacchi, Phys. Rev. B **79**, 165101 (2009).

[30] N. C. Wilson and S. P. Russo, Phys. Rev. B **79**, 094113 (2009).

[31] R. Grau-Crespo, A. Y. Al-Baitai, I. Saadoune, and N. H. de Leeuw, J. Phys. Condens. Matter **22**, 255401 (2010).

[32] E. Artacho *et al.*, J. Phys. Condens. Matter **20**, 064208 (2008).

[33] G. Poulet, P. Sautet, and E. Artacho, Phys. Rev. B **68**, 075118 (2003).

[34] G. Kresse and J. Furthmüller, Phys. Rev. B **54**, 11169 (1996).

[35] G. Kresse and J. Furthmüller, Comput. Mater. Sci. **6**, 15 (1996).

[36] E. Artacho, D. Sánchez-Portal, P. Ordejón, A. García, and J. M. Soler, Phys. Status Solidi B **215**, 809 (1999).

[37] J. M. Soler, E. Artacho, J. D. Gale, A. García, J. Junquera, P. Ordejón, and D. Sánchez-Portal, J. Phys. Condens. Matter **14**, 2745 (2002).

[38] T. C. Leung, C. T. Chan, and B. N. Harmon, Phys. Rev. B **44**, 2923 (1991).

[39] J. P. Perdew, K. Burke, and M. Ernzerhof, Phys. Rev. Lett. **77**, 3865 (1996).

[40] C. D. Latham, S. Öberg, P. R. Briddon, and F. Louchet, J. Phys. Condens. Matter **18**, 8859 (2006).

[41] V. Trinité, N. Vast, and M. Hayoun, J. Phys. Condens. Matter **20**, 235239 (2008).

[42] N. Troullier and J. L. Martins, Phys. Rev. B **43**, 1993 (1991).

[43] S. B. Fagan, R. Mota, A. J. R. da Silva, and A. Fazzio, Microelectron. J. **34**, 481 (2003).

[44] J. Izquierdo, A. Vega, L. C. Balbás, D. Sánchez-Portal, J. Junquera, E. Artacho, J. M. Soler, and P. Ordejón, Phys. Rev. B **61**, 13639 (2000).

[45] V. M. García-Suárez, C. M. Newman, C. J. Lambert, J. M. Pruneda, and J. Ferrer, Eur. Phys. J. B **40**, 371 (2004).

[46] J. Ortega-Castro, N. Hernández-Haro, A. Muñoz-Santiburcio, Hernández-Laguna, and C. I. Sainz-Díaz, J. Mol. Struct. (THEOCHEM) **912**, 82 (2009).

[47] B. Winkler, J. D. Gale, K. Refson, D. J. Wilson, and V. Milman, Phys. Chem. Miner. **35**, 25 (2008).

[48] J. Junquera, Ó. Paz, D. Sánchez-Portal, and E. Artacho, Phys. Rev. B **64**, 235111 (2001).

[49] V. I. Anisimov and O. Gunnarsson, Phys. Rev. B **43**, 7570 (1991).

[50] S. L. Dudarev, G. A. Botton, S. Y. Savrasov, C. J. Humphreys, and A. P. Sutton, Phys. Rev. B **57**, 1505 (1998).

[51] A. D. Becke, J. Chem. Phys. **98**, 1372 (1993).

[52] J. P. Perdew and M. Ernzerhof, J. Chem. Phys. **105**, 9982 (1996).

[53] J. P. Perdew and A. Zunger, Phys. Rev. B **23**, 5048 (1981).

[54] A. Svane and O. Gunnarsson, Phys. Rev. Lett. **65**, 1148 (1990).

[55] I. P. R. Moreira, F. Illas, and R. L. Martin, Phys. Rev. B **65**, 155102 (2002).

[56] K. N. Kudin, L. Scuseria, and R. L. Martin, Phys. Rev. Lett. **89**, 266402 (2002).

[57] P. J. Hay, R. L. Martin, J. Uddin, and G. E. Scuseria, J. Chem. Phys. **125**, 034712 (2006).

[58] I. D. Prodan, G. E. Scuseria, J. A. Sordo, K. N. Kudin, and R. L. Martin, J. Chem. Phys. **123**, 014703 (2005).

[59] P. Rivero, I. P. R. Moreira, G. E. Scuseria, and F. Illas, Phys. Rev. B **79**, 245129 (2009).

[60] G. I. Csonka, J. P. Perdew, A. Ruzsinszky, P. H. T. Philipsen, S. Lebegue, J. Paier, O. A. Vydrov, and J. G. Angyan, Phys. Rev. B **79**, 155107 (2009).

[61] K. Yang, J. Zheng, Y. Zhao, and D. G. Truhlar, J. Chem. Phys. **132**, 164117 (2010).

[62] O. A. Vydrov and G. E. Scuseria, J. Chem. Phys. **125**, 234109 (2006).

[63] A. V. Krukau, G. E. Scuseria, J. P. Perdew, and A. Savin, J. Chem. Phys. **129**, 124103 (2008).

[64] T. M. Henderson, B. G. Janesko, and G. E. Scuseria, J. Phys. Chem. **112**, 12530 (2008).

[65] J. Heyd, G. E. Scuseria, and M. Ernzerhof, J. Chem. Phys. A **118**, 8207 (2003).

[66] J. Heyd and G. E. Scuseria, J. Chem. Phys. **121**, 1187 (2004).

[67] J. E. Peralta, J. Heyd, G. E. Scuseria, and R. L. Martin, Phys. Rev. B **74**, 073101 (2006).

[68] E. N. Brothers, A. F. Izmaylov, J. O. Normand, V. Barone, and G. Scuseria, J. Chem. Phys. **129**, 011102 (2008).

[69] J. P. Perdew, A. Ruzsinszky, J. M. Tao, V. N. Staroverov, G. E. Scuseria, and G. I. Csonka, J. Chem. Phys. **123**, 062201 (2005).

[70] A. Rohrbach, J. Hafner, and G. Kresse, Phys. Rev. B **70**, 125426 (2004).

[71] M. Cococcioni and S. de Gironcoli, Phys. Rev. B **71**, 035105 (2005).

[72] H. J. Monkhorst and J. D. Pack, Phys. Rev. B **13**, 5188 (1976).

[73] F. Birch, Phys. Rev. **71**, 809 (1947).

[74] J. F. Nye, *Physical Properties of Crystals* (Oxford University Press, New York, 1985).

[75] H. B. Guo, J. H. Li, L. T. Kong, and B. X. Liu, Phys. Rev. B **72**, 132102 (2005).

[76] Y. Kong, W. Xiong, H. Guo, W. Sun, Y. Du, and Y. Zhou, CALPHAD **34**, 245 (2010).

[77] P. Pou, F. Flores, J. Ortega, R. Pérez, and A. L. Yeyati, J. Phys. Condens. Matter **14**, L421 (2002).

[78] A. V. Postnikov, G. Bihlmayer, and S. Blügel, Comput. Mater. Sci. **36**, 91 (2006).

[79] H. Zhang, M. P. J. Punkkinen, B. Johansson, S. Hertzman, and L. Vitos, Phys. Rev. B **81**, 184105 (2010).

[80] C. Kittel, *Introduction to Solid State Physics*, 7th ed. (Wiley, New York, 1996).

[81] P. H. T. Philipsen and E. J. Baerends, Phys. Rev. B **54**, 5326 (1996).

[82] J. A. Rayne and B. S. Chandrasekhar, Phys. Rev. **122**, 1714 (1961).

[83] J. J. Adams, D. S. Agosta, R. G. Leisure, and H. Ledbetter, J. Appl. Phys. **100**, 113530 (2006).

[84] J. Behler, Ph.D. thesis, Von der Fakultät II-Mathematik und Naturwissenschaften der Technischen Universität Berlin (2004).

[85] O. Gunnarsson and R. O. Jones, Phys. Rev. B **31**, 7588 (1985).

[86] *CRC Handbook of Chemistry and Physics*, 87th ed., edited by D. R. Lide (Taylor and Francis, Boca Raton, FL, 2007), internet version.

[87] F. J. Morin, Phys. Rev. **78**, 819 (1950).

[88] C. Greaves, J. Solid State Chem. **49**, 325 (1983).

[89] Z. Somogyvári, E. Sváb, G. Mészáros, K. Kreznov, I. Nedkov, I. Sajó, and F. Bourée, Appl. Phys. A **74**, S1077 (2002).

[90] A. F. Gualtieri and P. Venturelli, Am. Mineral. **84**, 895 (1999).

[91] T. Nagai, H. Kagi, and T. Yamanaka, Am. Mineral. **88**, 1423 (2003).

[92] A. E. Gleason, R. Jeanloz, and M. Kunz, Am. Mineral. **93**, 1882 (2008).

[93] H. Christensen and A. N. Christensen, Acta Chem. Scand. A **32**, 87 (1978).

[94] E. J. Ewing, J. Chem. Phys. **3**, 420 (1935).

[95] A. Oleś, A. Szytuła, and A. Wanic, Phys. Status Solidi B **41**, 173 (1970).

[96] E. J. W. Verwey, Nature (London) **144**, 327 (1939).

[97] F. Walz, J. Phys. Condens. Matter **14**, R285 (2002).

[98] M. Mizoguchi, J. Phys. Soc. Jpn. **44**, 1501 (1978).

[99] M. Mizoguchi, J. Phys. Soc. Jpn. **44**, 1512 (1978).

[100] P. Novák, H. Štěpánková, J. Englich, J. Kohout, and V. A. M. Brabers, Phys. Rev. B **61**, 1256 (2000).

[101] J. P. Wright, J. P. Attfield, and P. G. Radaelli, Phys. Rev. B **66**, 214422 (2002).

[102] S. B. Wilkins, S. DiMatteo, T. A. W. Beale, Y. Joly, C. Mazzoli, P. D. Hatton, P. Bencok, F. Yakhou, and V. A. M. Barbers, Phys. Rev. B **79**, 201102R (2009).

[103] Y. Miyamoto and M. Shindo, J. Phys. Soc. Jpn. **62**, 1423 (1993).

[104] J. Majzlan, K.-D. Grevel, and A. Navrotsky, Am. Mineral. **88**, 855 (2003).

[105] W. Zhang, J. R. Smith, and X.-G. Wang, Phys. Rev. B **70**, 024103 (2004).

[106] H. Guo and Y. Qi, Modell. Simul. Mater. Sci. Eng. **18**, 034008 (2010).

[107] *JANAF Thermochemical Tables*, 3rd ed., edited by M. W. Chase (ACS, Washington, DC, 1985).